Study of Modeling Neutron Interactions in the SuperFGD Prototype Through Simulation

A Thesis Presented

by

Harrison Wolf

to

The Graduate School

in Partial Fulfillment of the Requirements

for the Degree of

Master of Arts

in

Physics

Stony Brook University

May 2025

Stony Brook University

The Graduate School

Harrison Wolf

We, the thesis committee for the above candidate for the Master of Arts degree, hereby recommend acceptance of this thesis.

Chang Kee Jung – Thesis Advisor
Distinguished Professor, Department of Physics and Astronomy

Ciro Riccio – Thesis Co-Advisor
Assistant Professor, Department of Physics and Astronomy

Ross Corliss – Chairperson of Defense
Research Assistant Professor, Department of Physics and Astronomy

Maria Gonzalez-Garcia
Professor, Department of Physics and Astronomy

Alexandre Abanov
Professor, Department of Physics and Astronomy

This thesis is accepted by the Graduate School.

Celia Marshik
Dean of the Graduate School

Abstract

Long baseline (LBL) neutrino oscillation experiments are continuously pushing towards new frontiers of high energy physics. To continue pushing boundaries, systematic uncertainties on various experimental parameters must be reduced. Neutrons are among the largest sources of systematic uncertainty in neutrino energy measurement. In this work, we present a study of the simulation of a neutron beam and its interactions with a prototype of the Super Fine Grained Detector (SuperFGD) installed in the Tokai to Kamioka (T2K) LBL experiment. Some results of this simulation are compared with data taken at Los Alamos National Laboratory (LANL) in 2019. We provide an in-depth description of neutron interactions and their simulation, the SuperFGD's conceptual design and systematics, and studies performed to refine the reconstruction and analysis procedure.

Contents

Acknowledgments

To my parents: Thank you for always being by my side. I could not, in a million years, begin to express my full gratitude for the endless support you have given me and for raising me to be my fullest self.

To my grandparents: Thank you for your unconditional love. I still may not be able to explain the practical uses for my work, but I will always strive to follow in your footsteps and leave this world better than I found it.

To my friends: Thank you for lifting me up through lows and highs. Alex (Zhu and Landry), Aidan, Jack, Griffin, Tim, Kyle, Kuunal, Gabe, Dathan, Daniel, Evan, Tanner, Sean, Will, and a hundred other people–I will cherish every moment spent with those I have the privilege of calling my friends.

To Ciro: Thank you for teaching me to be a researcher. Thank you for being patient with me, for meeting me where I am and always giving me the tools to succeed. I hope that you have seen in me the growth that I have felt. There will be many problems on the road ahead of me; may I always have the wisdom to approach them with your advice in mind.

To Chang Kee and the NN group: Thank you for giving me the chance to make my time in this program meaningful. In my two short years at Stony Brook, the opportunities afforded to me while working in this group are more than I could have dreamed of.

To Dr. Roy Briere: Thank you for taking me on my first steps into the world of high energy physics. I didn't know at the time just what I was getting myself into, but 4 years later I'm ready to follow this road to wherever it takes me.

To the members of my thesis defense committee: Thank you for taking the time out of your busy lives to commemorate this milestone with me. I have poured my heart, soul, and a little bit extra into this work–I truly hope that

it shows.

Finally, to whoever is reading this, whether you were listed above or not: Thank you for reading. This thesis was a labor of love. Thank you for joining me on this journey.

Introduction

The T2K experiment is concerned with long-baseline neutrino oscillations, specifically measurements of the oscillation angles θ_{13} and θ_{23} and CP violating phase. In order to get an accurate measurement of these parameters, we must know the neutrino oscillation probability to fit our results against the known theory. Besides the oscillation angles and phase, the neutrino energy and distance it travels are the "experimental" parameters of neutrino oscillation. The baseline length is well-known for the T2K experiment, so it remains to accurately measure the neutrino energy. The near detector complex for T2K (ND280) is well-equipped to measure the neutrino flux and event rate of interactions involving neutrinos and secondary particles. This informs the far detector (SuperKamiokande) in their reconstruction of neutrino energies. However, one large source of "missing" energy remains: energy carried by neutrons, which account for approximately 10% of the neutrino energy when they are produced. Neutrons can be produced by charged-current quasi-elastic (CCQE) antineutrino interactions or from secondary/final state neutrino interactions. Before installation of the SuperFGD, ND280 had only two plastic scintillator grids–the Fine Grained Detector (FGD)–sandwiched between 3 Time Projection Chambers (TPCs) in order to measure neutron energies. This proved insufficient, as the 2D scintillation bars did not give enough granularity to track down neutron interactions. This is doubly true since neutrons do not produce scintillation light–they can only be tracked down from other (charged) particles that they produce.

The Super Fine Grained Detector (SuperFGD) seeks to solve this issue by introducing a segmented 3D scintillation tracker. The detector is composed of cubes of 1 cm made of scintillating plastic. Each of these cubes has 3 orthogonal wavelength shifting fibers to carry photoelectrons to 3 (x, y, z) planes of multi-pixel photon counters (MPPCs). This allows the SuperFGD to obtain quasi-3D event reconstruction by combining information across 3 readout planes. Two prototypes of this detector were created: the SuperFGD prototype and the US-Japan (US-JP) prototype. This work will focus only on the prior, specifically on its testing at the Weapons Neutron Research Facility

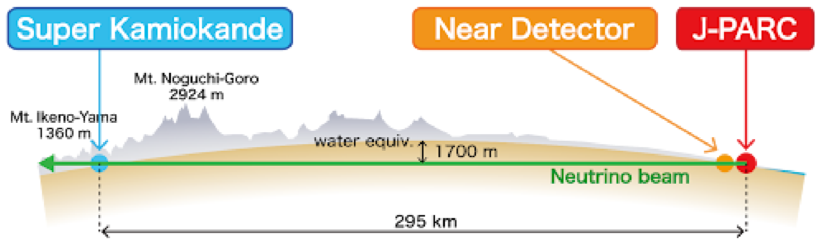

Figure 1: An illustration of the T2K near detector and far detector setup. J-PARC refers to the Japan Proton Accelerator Research Complex, where T2K's neutrino beam is produced. [1]

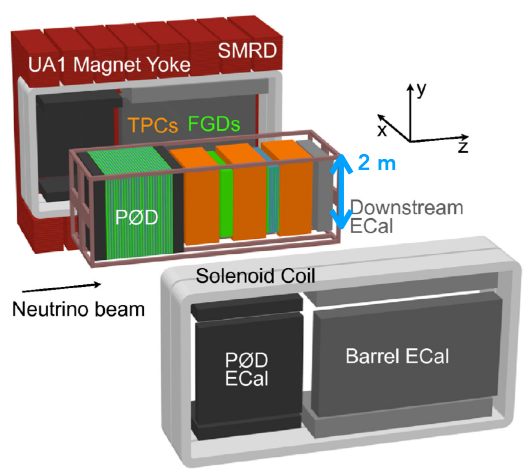

Figure 2: The old ND280 experimental setup. Note the TPCs in light green. [2]

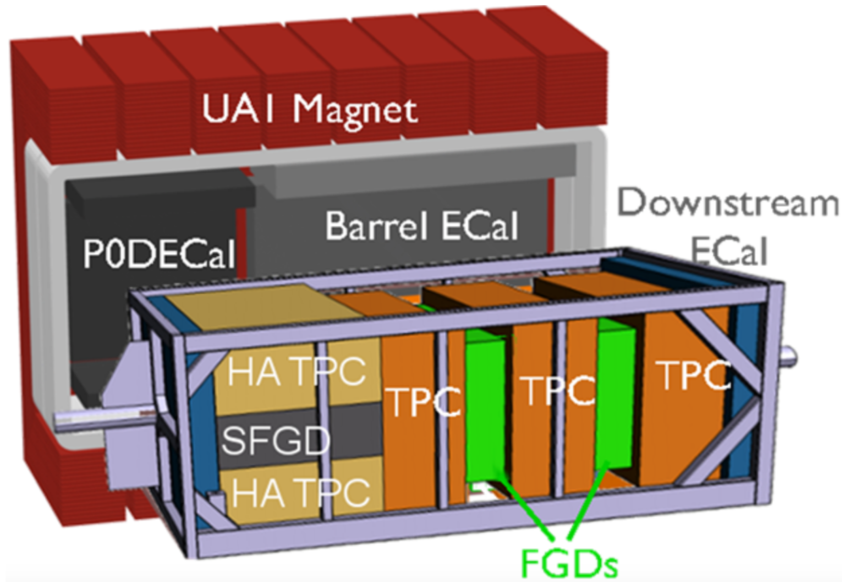

Figure 3: A scheme of the new ND280 experimental setup. The SuperFGD and new High-Angle TPCs (HATPC) were installed in place of the π_0 Detector (PØD above). [3]

(WNR) at Los Alamos National Laboratory (LANL).

It is important to note at this point the frontiers that the SuperFGD is pushing towards: it is the first detector in high energy physics to be able to measure neutron kinematics, specifically neutron energy, on an event-by-event basis. This is only achievable via the detector's segmented design, allowing for time resolutions on the order of a few nanoseconds and spatial resolutions smaller than a centimeter. As will be discussed later, neutrons are among the most difficult particles to detect. Thus, the SuperFGD represents a huge leap forward in detector capabilities for particle physics.

This thesis will present a study on neutron simulation and the neutron interaction cross-section and its comparison to data collected in the SuperFGD prototype tests conducted in 2019. Since T2K nominally operates at a neutrino energy peaked around 600 MeV, neutrons of energies 0-800 MeV were studied in these tests. Note that all simulations presented in this work were created with the Geant4 particle simulation software. Two physics lists were primarily used, Bertini and INCLXX, with the ultimate goal of testing and tuning them in tandem with our simulation and analysis chain. Some results will be presented for both physics lists.

In chapter 1, we will discuss the specifics of neutron interactions both in general and in the SuperFGD before moving on to a description of the Geant4 simulation software and how it handles neutron interactions. In chapter 2, we will move to an in-depth description of the SuperFGD prototype and the experimental setting of the neutron beam tests at LANL. Finally, in chapter 3, we will discuss the specifics of analyzing neutron events in the SuperFGD prototype and present the results of our simulation analysis in comparison to data.

Chapter 1

Neutron Interactions: Modeling and Simulation

1.1 Neutron Energy Categories

Neutrons, having no charge, cannot interact with matter via the Coulomb force. For charged particles, Coulomb interactions are the primary mechanism of energy loss during travel. Thus, without these interactions, neutrons can only interact with matter hadronically, i.e. directly with the nucleus of the detector material. This interaction is mediated by the strong nuclear force: the very short effective range ($\approx 10^{-13}$ m) of this force means that neutron interactions are much rarer than charged particle interactions. This reaffirms the T2K experiment's issues with detecting and reconstructing neutron energy– neutrons may be completely invisible to many small detectors.

Neutron interactions vary greatly depending on the neutron's energy, sometimes also known as "temperature". For completeness, we will list here all of the neutron energy classifications, but only a few will be relevant for later discussions regarding the SFGD prototype. The energy ranges and typical names are as follows [4]:

At a given temperature T, neutrons will have a Maxwell-Boltzmann energy distribution around the energy $k_B T$. At room temperature ($\approx 300K$) this energy is equal to 0.025 eV. Thus, the nomenclature of cold and thermal reflects the neutron's mean energy relative to typical room temperature environments.

Cold neutrons are rare outside of dedicated nuclear reactors. They occur only when brought into thermal equilibrium with liquid nitrogen or another similarly cold fluid. Thermal neutrons are in thermal equilibrium with a room temperature environment. Both of these types have a high effective absorption cross section with the material they are in thermal equilibrium with. This ab-

Cold	0-0.025 eV
Thermal	0.025 eV-0.4 eV
Cadmium	0.4-1 eV
Slow	1-10 eV
Resonance	10-300 eV
Intermediate	300 eV-1 MeV
Fast	1-20 MeV
Ultrafast/relativistic	>20 MeV

Table 1.1: List of main neutron interaction categories by energy range.

sorption will create a radioactive isotope of the absorbing nucleus–this process is known as "neutron activation".

The upper bound of the thermal range and thus the lower bound of the "Cadmium" neutron range is of some significance. The neutron absorption cross section of the isotope Cadmium-113 is very large at energies below 0.5 eV and drops off rapidly as the energy increases [4], indicated in Fig. 1.1. In more detailed studies of neutron passage through matter, this is known as the "cadmium cutoff". This is of note because this significant difference in behavior makes Cadmium a prime candidate for selective absorption, allowing one to effectively separate <0.5 eV neutrons from those above this threshold.

Slow neutrons are when nuclear resonances can begin to take place within certain elements and isotopes. However, this does not become a prominent effect until the aptly named "resonance" energy range. Here, most nuclei have many resonances, sometimes spaced by less than 1 eV. For sufficiently low energies and wide enough spacing, these resonances may be individually resolved. However, once the neutron passes into the intermediate energy region, the resonance spacing becomes smaller and smaller compared to the neutron energy. Thus, there are many nuclei for which the resonance spectrum cannot be resolved. In these cases, we may only measure the average interaction cross section.

At around 1 MeV, neutrons may participate in nuclear reactions in which other particles are created and ejected from the nucleus, such as protons and α particles. Additionally, neutrons that are produced through nuclear interactions tend to have energies on the MeV scale. Above 20 MeV, neutrons become relativistic: a 20 MeV neutron has a velocity of $0.2c$. In this work we focus on ultrafast neutrons.

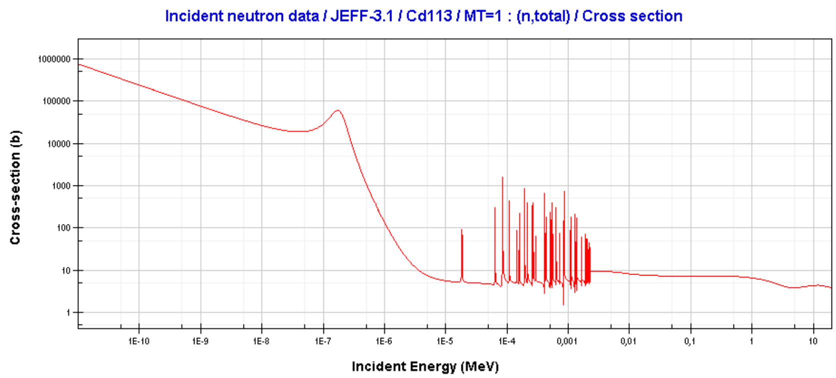

Figure 1.1: Neutron cross section on Cadmium-113. Note the cadmium cutoff and resonances beginning at ≈100 eV. These resonances are resolvable until the neutron energy is past 1 KeV. [5]

1.2 Neutron Interaction Modes

Having sufficiently described the way we can categorize neutron energies, we can move to describing their interactions. A simple and common interaction is elastic scattering, in which the target nucleus will recoil (and thus reduce the neutron energy) but remain in the ground state. For any non-fast neutron ($\lesssim$ 1 MeV), the de Broglie wavelength is large compared to the nuclear radius. This means that the scattering can be treated as isotropic in the center of mass frame. We find that the neutron loses an average energy

$$E_{lost} = \frac{2A}{(A+1)^2}E \tag{1.1}$$

where A is the mass number of the target nucleus. It is common for an intermediate neutron to undergo many elastic collisions in succession, losing energy until it becomes thermal and is absorbed. This process is known as "neutron moderation".

Any interaction other than this simple collision is termed inelastic. As discussed above, intermediate neutrons may induce excitation in the target nucleus, bringing it into an excited state. This becomes more common as the neutron energy increases. Oftentimes an inelastic interaction will result in neutron capture and the subsequent decay of the excited compound nucleus through γ-ray radiation, known as "radiative capture". The cross section for this process is denoted, for a carbon target, as C(n,nγ)C in Fig. 1.2. Inelastic reactions caused by fast or ultrafast neutrons may, as mentioned above, also produce protons, pions, or α particles in the final state, among a number of

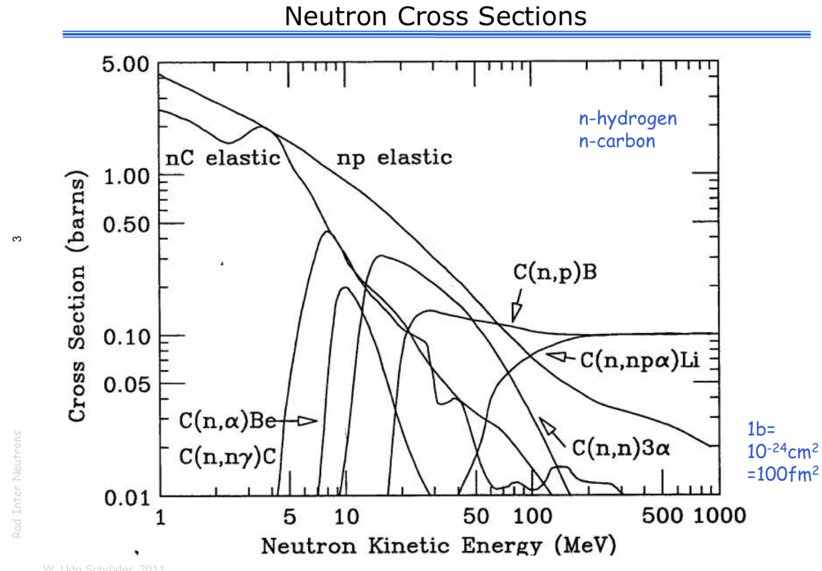

Figure 1.2: Elastic and inelastic (radiative capture, nuclear proton emission, partial/complete fragmentation) neutron cross sections on hydrocarbon. [6]

other particles depending on the target nucleus. The cross section for proton emission from a carbon atom is labeled as C(n,p)B in Fig. 1.2. To determine whether a specific particle or set of particles can be created from a neutron interaction, we can calculate the threshold energy for a creation process. This is a simple calculation from momentum conservation and we find, in natural units (c = 1)

$$E_{min} = \frac{(\Sigma_{i=0} m_i)^2 - (\Sigma_{j=0} m_j)^2}{2m_N} \tag{1.2}$$

Where i denotes the initial state particles (neutron and target), j denotes the final state particles, and m_N is the neutron mass.

In extreme cases, the target nucleus may break apart completely in a process called fragmentation. For example, a Carbon-12 nucleus may be fragmented into 3 α particles. Cross sections for inelastic reactions typically go as $1/v$ at leading order [4], with v being the neutron velocity. The cross section for carbon fragmentation is labeled as C(n,n)3α in Fig. 1.2.

1.3 Neutron Cross Sections

Cross sections for a certain production process have an intuitive quantitative description in terms of the distribution of occurrence for a certain reaction product [7]: The cross section for a product p can be defined as

$$\sigma_p = \frac{\text{number of particles } p \text{ produced per unit time}}{\text{number of incident particles per unit area per unit time}} \tag{1.3}$$

From this, we can see that cross sections have dimensions of area. Typically, this is measured in cm^2 or, more commonly in particle physics, the barn, where $1 \text{ barn} = 10^{-24} \text{ cm}^2$.

The cross section is highly dependent on the internal structure of the target nucleus. This fact itself leads to a broad field of study in nuclear physics– we can compare experimental scattering observables with calculations from various nuclear models. This can help us reveal which of these models best reflects the reality of the internal nuclear structure.

Focusing now on interactions with only a neutron projectile, we can quantify the rate of neutron interactions with the total cross section, given simply as the sum of the cross sections for unique products

$$\sigma_{tot} = \sigma_{elastic} + \sigma_{inelastic} + \sigma_{capture} + \ldots \tag{1.4}$$

We can determine the probability for a neutron to interact per unit of length (inverse mean free path length) by combining this cross section with the density of atoms in a material, N_{atoms}, and the fact that neutrons can only interact directly with a target nucleus

$$\lambda = N_{atoms}\sigma_{tot} = \frac{N_A\rho}{A}\sigma_{tot} \tag{1.5}$$

where N_A is Avogadro's number, ρ is the material density, typically in g/cm^3, and A is again the mass number for the target nucleus. This simple expression for the inverse mean free path tells us that a narrow neutron beam will be exponentially attenuated while passing through a material [8]. Thus, if we start with some number of neutrons N_0, we will find at some length z through the detector

$$N = N_0 e^{-\lambda z} \tag{1.6}$$

Note that we have used σ_{tot} in the expression for λ. However, λ is in fact constant for any one of the interaction mechanisms listed above, and thus the exponential attenuation will still be valid. For the purpose of this work, this fact allows us to make an arbitrary selection of neutron interaction modes and final state configurations, that we refer to as "topologies", with which to reconstruct the neutron interaction cross section. See the discussion of single-track event selection in Chapter 3 for more details.

1.4 Neutron Interactions on Hydrocarbon

As mentioned before, the SuperFGD prototype is a plastic (hydrocarbon) scintillator detector that was tested at neutron energies ranging from 0-800 MeV. Further properties of the detector setup will be explored in Chapter 2. We will now discuss neutron interactions on hydrogen and carbon on their own to gain some more context for our expectations for modeling and simulation.

1.4.1 Neutron Interactions on Hydrogen

First, we will consider elastic interactions. An elastic interaction of a neutron with a free proton (hydrogen nucleus) can be treated classically. Thus, the dynamics of the interaction will be sufficiently modeled with familiar "billiard ball" scattering equations from classical mechanics.

In this case, Eq. (1.1) may be used. For $A = 1$, we see that the average energy lost in an elastic interaction on hydrogen is exactly 1/2 of the neutron's incoming energy. We can also calculate the fractional energy lost to this interaction more precisely, but we first must consider the angular distribution of this scattering process.

Classical kinematical analysis gives us the following relationship for the angle between two outgoing objects after an elastic collision

$$\phi = \arccos \frac{|\boldsymbol{v_2}|(\frac{m_2}{m_1} - 1)}{2|\boldsymbol{v_1}|} \tag{1.7}$$

Where m_1 is the neutron mass, m_2 is the target mass (in this case a proton), and $|\boldsymbol{v_1}|$ and $|\boldsymbol{v_2}|$ are their respective velocity magnitudes after the interaction takes place (boldface indicates a vector quantity). Since the neutron and proton have very similar masses, we would expect their relative angle to be very close to 90° no matter the outgoing velocities.

To calculate the neutron's fractional energy loss, we must consider the angle an outgoing neutron makes with respect to the beam rather than the target. After all, a neutron may only have a glancing interaction with a proton, after which the proton will be recoiled near 90° with respect to the beam, but at very little energy cost to the neutron. Another classical analysis yields the following relationship for the fractional energy loss Q

$$Q = \frac{4m_1m_2}{(m_1+m_2)^2}\cos^2(\beta) \tag{1.8}$$

where m_1 and m_2 are again the masses of the particles involved and β is the angle the outgoing neutron makes with respect to the beam. By setting $\beta = 0 \rightarrow \cos(\beta) = 1$ in Eq. (1.8), we find the maximum fractional energy loss

$$Q_{max} = \frac{4m_1m_2}{(m_1+m_2)^2} \tag{1.9}$$

Once again, since the proton and neutron masses are very similar, we find that the neutron may impart nearly all of its energy to the proton, recoiling the neutron at a near 90° angle, as expected.

Now we will consider inelastic interactions. In the energy range of interest, inelastic scattering of neutrons on protons may produce pions. These processes can be verified to conserve all the relevant quantum numbers, and therefore possible to achieve. We can use Eq. (1.2) to calculate the minimum energy required for these production processes to occur. Once again we will use natural units, taking the neutron mass to be 939 MeV and the proton mass to be 938 MeV.

- $n + p \rightarrow n + p + \pi^0 \Rightarrow E_{min} = 279$ MeV
- $n + p \rightarrow D + \pi^0 \Rightarrow E_{min} = 275$ MeV
- $n + p \rightarrow n + n + \pi^+ \Rightarrow E_{min} = 290$ MeV
- $n + p \rightarrow p + p + \pi^- \Rightarrow E_{min} = 286$ MeV

Here, D represents a deuteron. Note that since these are the minimum energies for these processes to occur, all of the products will be created at rest at these energies.

We can go one step further and calculate the expected production ratio of, for example, π^+ and π^- through these channels. This calculation can be performed rather simply using the Clebsch-Gordan decomposition of the relevant isospin states.

Consider a combined isospin state of a neutron and a proton. Recall that the isospin state for a particle is given as $|I, I_3\rangle$, where I is the particle's spin and $I_3 = \frac{1}{2}(n_u - n_d)$, with n_u and n_d being the number of up and down quarks contained within the particle, respectively. Then a neutron has an isospin state $|1/2, -1/2\rangle$, whereas a proton has $|1/2, 1/2\rangle$. The tensor product of these two states gives the initial isospin state of the neutron-proton system:

$$|1/2,1/2\rangle \otimes |1/2,-1/2\rangle = \frac{1}{\sqrt{2}}(|0,0\rangle + |1,0\rangle) \tag{1.10}$$

By taking the inner product of this state with the relevant final state and squaring the result, we can find ratios between two such final states. Since all other factors are the same between the two processes, this ratio will give the ratio of the cross-sections for the channels.

Consider a state composed of two neutrons and a π^+. This is represented by the state

$$|1/2,-1/2\rangle \otimes (|1/2,-1/2\rangle \otimes |1,1\rangle) \tag{1.11}$$

We will assume that the reader is familiar with Clebsch-Gordan decomposition and skip the details of that calculation along with the algebra that follows. The final representation of the state is given by

$$-\frac{1}{\sqrt{3}}|0,0\rangle - \left(\frac{1}{\sqrt{3}} + \frac{1}{\sqrt{6}}\right)|1,0\rangle + \frac{1}{\sqrt{6}}|2,0\rangle \tag{1.12}$$

Then, taking the basis to be orthonormal, the inner product of the initial neutron-proton state with this final state is simply $-\frac{2}{\sqrt{6}} - \frac{1}{\sqrt{12}}$.

Similarly, the final state composed of two protons and a π^- has the isospin state

$$|1/2,1/2\rangle \otimes (|1/2,1/2\rangle \otimes |1,-1\rangle) = \frac{1}{\sqrt{3}}|0,0\rangle + \left(\frac{1}{\sqrt{3}} + \frac{1}{\sqrt{6}}\right)|1,0\rangle + \frac{1}{\sqrt{6}}|2,0\rangle \tag{1.13}$$

Note that this state is, up to an overall sign in the first two terms, identical to the isospin state for two neutrons and a π^+. So, when we take the inner product of this state with the initial state, we find $\frac{2}{\sqrt{6}} + \frac{1}{\sqrt{12}}$, exactly the negative of our prior result. Thus, when squaring these quantities and taking the ratio, we find

$$\frac{\sigma_{\pi^+ prod.}}{\sigma_{\pi^- prod.}} = \left|\frac{\langle n,p|n,n,\pi^+\rangle}{\langle n,p|p,p,\pi^-\rangle}\right|^2 = 1 \tag{1.14}$$

where we slightly abuse notation to represent the isospin states as simply containing the particles themselves. This calculation is a representation of isospin as an exact symmetry. However, as shown in Fig. 1.3, slight differences can be observed. The experimental deviations from the theory come from the different masses of the π^+ and π^-, which was excluded in the calculation above but would have entered only as a multiplicative prefactor. The same

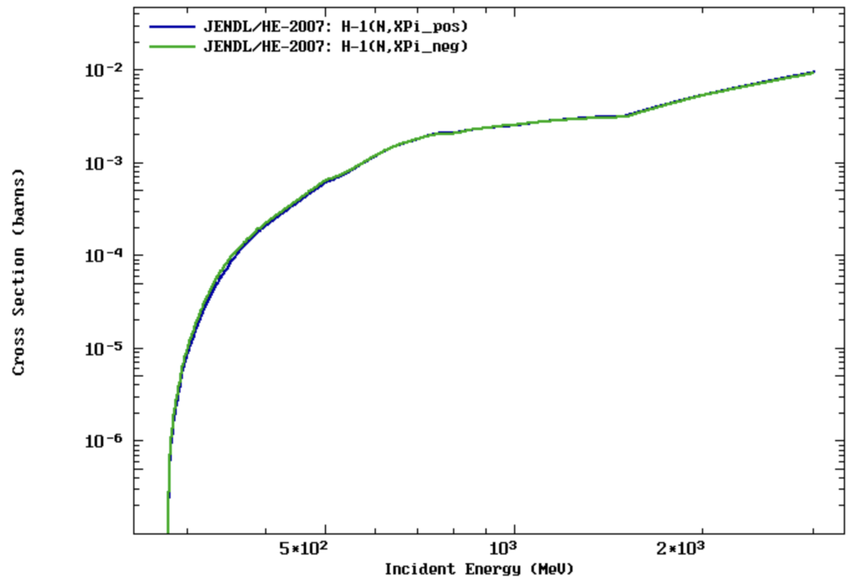

Figure 1.3: Charged pion production cross sections for neutrons incident on protons (H-1). As predicted, the cross sections are very nearly equal for all reported energy ranges. [9]

calculation can be performed for the $n + p + \pi^0$ final state; one finds that the ratio of π^0 production through this final state to either of the two final states discussed above is approximately 0.136.

1.4.2 Neutron Interactions on Carbon

Once again, we will first consider elastic scattering. If we treat this as a classical interaction, then we can use all of the previously derived equations and apply them to this system. With Carbon-12 as the target, Eq. (1.9) shows that $Q_{max} \approx 0.28E$. So, for a neutron with energy 800 MeV, we would expect to see carbon nuclei recoiling with a maximum energy of 224 MeV. Thus we now have an energy-transfer dependence in the relative angle between the products in this elastic collision: Using Eq. (1.7), we see that at maximum energy transfer the relative angle is restricted to the domain of $\phi \in [90°, 148°]$, whereas at lower energy transfers the relative angle may subsequently be lower. So, as opposed to interactions with hydrogen, neutron interactions with carbon may produce a neutron going backward in the detector.

The inelastic thresholds of note for neutron interactions on carbon in the SuperFGD prototype can be seen in Fig. 1.2. Eq. (1.2) may be used, but nuclear effects within the carbon nucleus complicate the calculation and the results from the simple production approximation may be off by up to an order of magnitude. This fact further emphasizes the need for simulation software which can make accurate predictions of physics occurring within the nucleus.

1.5 The Geant4 Simulation Software

Geant4 (also known throughout this work as Geant or G4) is a simulation toolkit that uses Monte Carlo methods to simulate the passage of particles through matter [10]. It is an extremely comprehensive software package, able to create a geometric model of any detector and its material, locate points and tracks within said model, apply the effects of various interactions and create the relevant secondary particles, visualize the detector and the tracks passing through it, and record true information from the simulation as hits to generate detector response.

The physics processes used for each interaction are collectively known as "physics lists". Geant4 has a wide compilation of physics lists that use various theoretical models of particle interactions. Many different use-cases are also covered, with physics lists designed to reduce computational power, enhance accuracy for particle transport in certain energy regions, or even provide optimal information for use in, e.g., medical or astrophysical environments.

Geant4 handles transport in discrete steps as particles move through the detector. Each particle in motion at each step is assigned all of the information we wish to collect. For example, a particle moving through our detector would be assigned an ID number based on its type, along with a track ID for the path it creates through the detector and, potentially, other variables such as its momentum and energy. At each step, G4 will determine if an interaction occurs based on the interaction cross section taken from the physics list used in the simulation (if an interaction with another particle does not occur, G4 can also handle particle decays). The cross section is used to generate a mean free path length given the detector material in the same way we formulated it above. At the point of interaction (or decay), the particle is given a process and subprocess ID, indicating which type of interaction occurred. The particle's trajectory is changed–if the interaction is elastic, the track ID associated with the projectile will be unchanged, but a new track ID will be given to the recoiling target. For an inelastic interaction, a new track ID is generated for all of the outgoing particles along with parent IDs to indicate which particles are associated with which interactions. Final state particles are then transported along through the detector in the same discrete steps as the initial projectile, and the process continues until all particles have exited the detector or deposited all of their energy until they are below a certain threshold beyond which Geant will no longer simulate them. At this point the

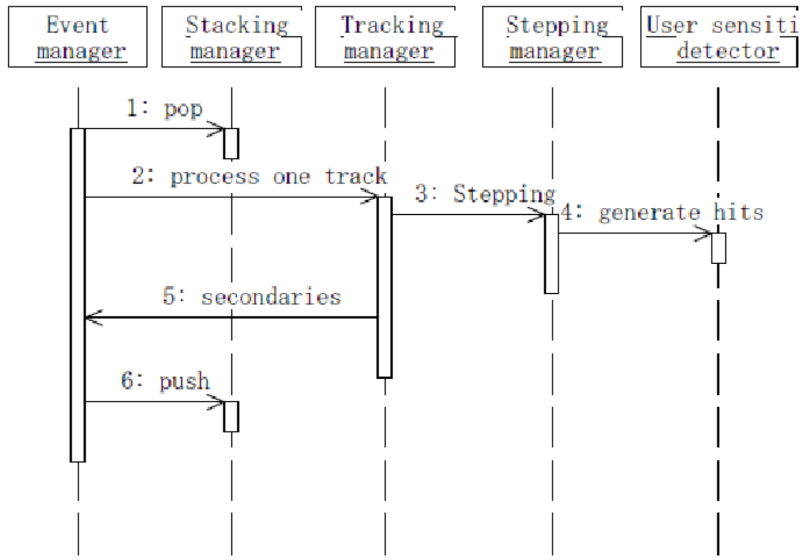

Figure 1.4: Diagram illustrating how Geant4 processes a single event. [10]

energy deposition of each primary and secondary particle is tabulated and the simulation will move on to a new event with a new primary projectile.

1.6 Neutron Interactions in Geant4

The entire discussion under this heading may be boiled down to an overview of how Geant4 retrieves the neutron interaction cross section. For a vast majority of HEP-focused physics lists, the class G4PARTICLEXS is used to access a compilation of cross sections on various targets. Like neutrons themselves, G4PARTICLEXS has separate models based on the neutron energy.

For neutrons below 20 MeV, the data-driven, isotope-specific G4NDL (G4 Neutron Data Library) is used to retrieve the neutron cross sections [11]. This results in a very simple parameterization of preexisting data based on datasets found in the ENDF (Evaluated Nuclear Data Files). Specifically, the most recent version of G4 uses the JEFF-3.3 dataset. Not much computational power is required to access and use these cross sections accurately, so sometimes this energy region is expanded upon in so-called "high precision" physics lists. For example, there exists a version of the Bertini physics list called Bertini High Precision (HP) which can more accurately model the final state of a neutron-nuclear interaction below 20 MeV.

For neutrons between 20 MeV and 90 GeV, the Barashenkov parameteri-

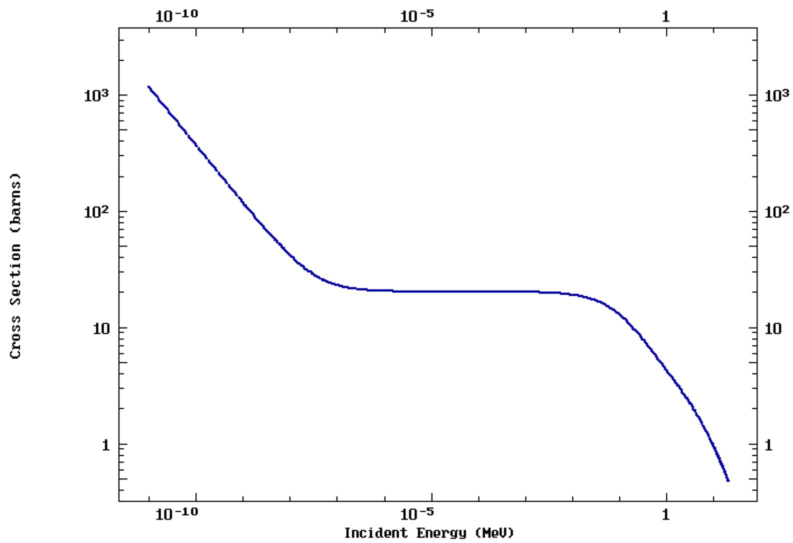

Figure 1.5: JEFF-3.3 cross section for neutrons on hydrogen. [12]

zation is used [13]. At energies below 1 GeV, particularly in the cases of light nuclei where the neutron's DeBroglie wavelength is only a few times smaller than the size of the target nucleus, a phenomenological expression is used

$$\sigma = \pi(r_0 A^{1/3} + \lambda)^2 \times f(E)\phi(A)^{\gamma(E)} \tag{1.15}$$

where A is the target atomic mass number, λ is the DeBroglie wavelength of the projectile, r_0 is a constant related to the radius of the target nucleus, and f, ϕ, and γ are empirical functions determined from data fits with constant adjusting parameters. At energies higher than 1 GeV, $\phi(A) \to A$ and $\gamma(E) \to$ constant.

For energies higher than 1 GeV, the cross section is derived with slightly more theoretical considerations. The optical model is employed, based on a solution of the Schrödinger equation with a phenomenological complex potential. The optical model is of great importance in nuclear physics for parametrizing prompt/direct reactions, i.e. any reaction that does not involve a compound intermediate state. We can use this since resonances are nonresolvable at high energies. Thus, we can use the same mean field to describe both bound and scattering states. This means that the optical model is only applicable to energy-averaged cross sections.

The reason that the scattering potential must be complex is to take into account the absorption of the "reaction flux" from the elastic scattering channel by the inelastic channel. This is analogous to the scattering and absorption of light by a complex refractive medium, hence the nomenclature of the optical model. The optical model and its various parameterizations for the nuclear potential are both mathematically rich and, unfortunately, beyond the scope of this work. We will present the Barashenkov parameterization here and leave the details to the curious reader [14].

$$\sigma_{elastic} = \frac{\lambda}{4\pi}\Sigma_l(2l+1)[1-e^{2i\eta_l l}]^2 \tag{1.16}$$

$$\sigma_{inelastic} = \frac{\lambda}{2\pi}\Sigma_l(2l+1)[1-e^{-4\chi_l}] \tag{1.17}$$

where l denotes the angular momentum state of the target nucleus (as spin-orbit considerations are taken into account) and η_l is the nuclear potential, with χ_l being its imaginary part

$$\eta_l = \delta_l + i\chi_l = \frac{1}{2}\int_{2\pi\lambda l}^{\infty} dr \frac{rn(r)}{\sqrt{r^2+(2\pi\lambda l)^2}} \tag{1.18}$$

where $n(r)$ is the intranuclear density. This density also has energy-dependent corrections, and its full form is given by

$$Re(n(r,E)) = A\xi_1(E)[\frac{Z}{A}\alpha_p(E)\sigma_p(E) + (1-\frac{Z}{A})\alpha_n(E)\sigma_n(E)]d(r) \tag{1.19}$$

$$Im(n(r,E)) = A\xi_2(E)[\frac{Z}{A}\sigma_p(E) + (1-\frac{Z}{A})\sigma_n(E)]d(r) \tag{1.20}$$

where now $d(r)$ is the pure intranuclear density (determined in electron scattering experiments), Z is the charge number of the target, the ξ_i are adjusting parameters, σ_p and σ_n are the total p-p and n-n cross sections, and α_p and α_n are the corresponding ratios of the real and imaginary parts of the elastic amplitude taken at zero scattering angle.

G4 has access to a lookup table of cross sections calculated with these formulas at various energies. When a cross section must be retrieved for an energy that does not exactly match one found in the table, G4 will perform an interpolation on the dataset to provide the value.

Above 90 GeV, the Glauber-Gribov parameterization is used [15]. This is a much more recent development than the Barashenkov parameterization, and thus was created with direct access to much more data to inform the fits. This results in a parameterization more separated from theory, but ultimately less reliant on tuning parameters which may not have physical meaning.

The Glauber-Gribov extension to the cross-section calculation is a rather simplified model. It assumes nucleons are point-like and distributed according

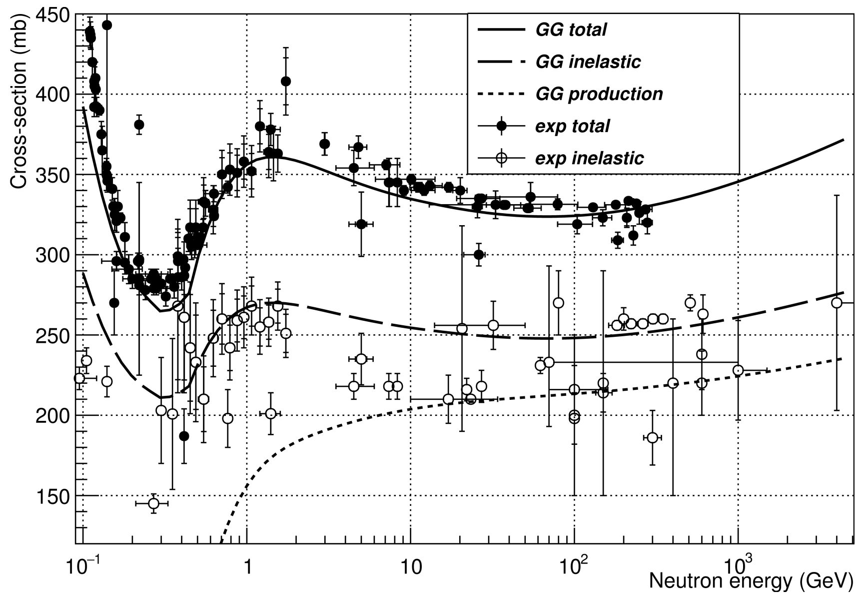

Figure 1.6: Glauber-Gribov cross sections for neutrons and protons on a carbon target. [15]

to a Gaussian probability distribution function within the nucleus. The cross-sections are calculated with the following equations:

$$\sigma_{tot}^{hA} = 2\pi R^2 \ln\left(1 + \frac{A\sigma_{tot}^{hN}}{2\pi R^2}\right) \tag{1.21}$$

$$\sigma_{inel}^{hA} = \pi R^2 \ln\left(1 + \frac{A\sigma_{tot}^{hN}}{\pi R^2}\right) \tag{1.22}$$

where h represents a hadron, A is the target mass number, and N represents a nucleon. The radius parameter R is a function of A. It then follows that $\sigma_{el}^{hA} = \sigma_{tot}^{hA} - \sigma_{inel}^{hA}$. This model reduces the free parameters to only σ_{tot}^{hN} and $R(A)$. These values can, in general, be provided by the Particle Data Group (PDG) or by Geant4 directly. The parameterization can be simplified further by noting that

$$A\sigma_{tot}^{hN} = N_p\sigma_{tot}^{hp} + N_n\sigma_{tot}^{hn} \tag{1.23}$$

where N_p and N_n are the number of protons and neutrons in the nucleus, respectively.

The nuclear radius is parameterized proportionally to the cube root of the mass number by

$$R(A) = r_0 A^{1/3} f(A) \tag{1.24}$$

with $r_0 \approx 1.1$ fm and $f(A) < 1$ for $A > 21$ and $f(A) > 1$ for $3 < A < 21$.

1.7 Physics Lists

Bertini [16] and INCL [17] refer to the two physics lists used in the Geant4 simulations produced for this work. They are both intranuclear cascade models, meaning that they seek to model effects which occur inside the nucleus of a target material. This process occurs largely in two parts: hard nucleon-nucleon collisions resulting in the emission of fast particles followed by de-excitation of the remnant nucleus. For the second stage of this process, the two models in question refer to further de-excitation/evaporation codes. The Bertini model includes these codes in its working package, while INCL does not. However, INCL is very typically coupled to the ABLA evaporation-fission model. In this section, we will give brief reviews of each model to better understand how they seek to achieve the goal of executing the first phase of the intranuclear cascade process.

1.7.1 The Bertini Cascade Model

The Bertini model is a so-called "space-like" intranuclear cascade model [18]. This means that collisions are based on the space that the projectile and target nucleons occupy in the nucleus; the collision site is determined by a correlation between a random number and the probability to interact based on partial integration of the inverse mean free path length. In the Bertini model, the mean free path length calculation relies on parameterized free-space cross sections, meaning that the sampled interaction points are not influenced by nuclear effects. These effects are taken into account later by the inclusion of Pauli blocking, Fermi motion, nucleon repulsion, and the trailing effect.

After the first interaction, one of the "participants" is tracked and its next collision site is determined by the same partial integration as prior. This process continues until the chosen particle "dies", i.e. leaves the nucleus or falls below a certain energy cutoff. The other participants are treated in the same way, one after the other, until they all die.

The intranuclear cascade of hadrons (particularly nucleons) through the nucleus is an extremely complicated series of interactions. The Bertini model reduces this to a classical model, solving an average of the Boltzmann equation for the transport of a particle through a "gas" of nucleons. The approximation of the nuclear medium as a gas is valid if the effective nucleon size is small and there are few collisions. The range of applicability for such an approximation is 200 MeV $< E <$ 3 GeV, where E is the energy of the particle initiating the cascade.

The nuclear potential is represented by a set of concentric, constant density shells whose depths approximate a Woods-Saxon potential. The number of shells vary between 1 and 6 based on the atomic weight of the nucleus. The functional form for the outer shell edges of a three-shell nucleus is

$$r_i = c \ln \left(\frac{1 + e^{-\frac{R_N}{c}}}{\alpha_i} - 1 + R_N \right) \tag{1.25}$$

where $R_N = aA^{1/3} + bA^{1/3}$, c is proportional to the nuclear skin depth, and $\alpha_i = [0.7, 0.3, 0.01]$. The Fermi momentum $p_{F,i}$ is proportional to the cube root of the density of the ith shell calculated above and is used to calculate the potential felt by the nucleons traveling in that shell

$$V_{N,i} = \frac{p_{F,i}^2}{2M_N} + B_N(A, Z) \tag{1.26}$$

where B_N is the nucleon binding energy. This potential only applies to nucleons since it follows from Pauli exclusion for these particles. Other hadrons feel potentials with a constant depth over all shells.

1.7.2 The INCL Model

The Liège intranuclear cascade (INCL) model is, in contrast to the Bertini model, a so-called "time-like" intranuclear cascade model [18]. This type of model divides the Fermi sphere of momentum into n parts of equal volume and calculate the mean cross section and the mean velocity in each subvolume. Then, the probability for interaction is calculated for a collision to take place in a certain time interval. The cascades for each participant particle are simulated together, stepping along time intervals as they interact.

Since the model is not "space-like", the nuclear medium is given a constant potential well representing the nuclear mean field. Target nucleons are given random positions and momenta in agreement with Woods-Saxon and Fermi distributions respectively. Particles can be transmitted or reflected from the potential they feel–the radius of the potential is dependent on the particle momentum. The potential radius for particles with energy greater than the nucleon Fermi energy is taken to be the maximum radius of the "working sphere" that contains all interactions simulated by the model. That radius is given by

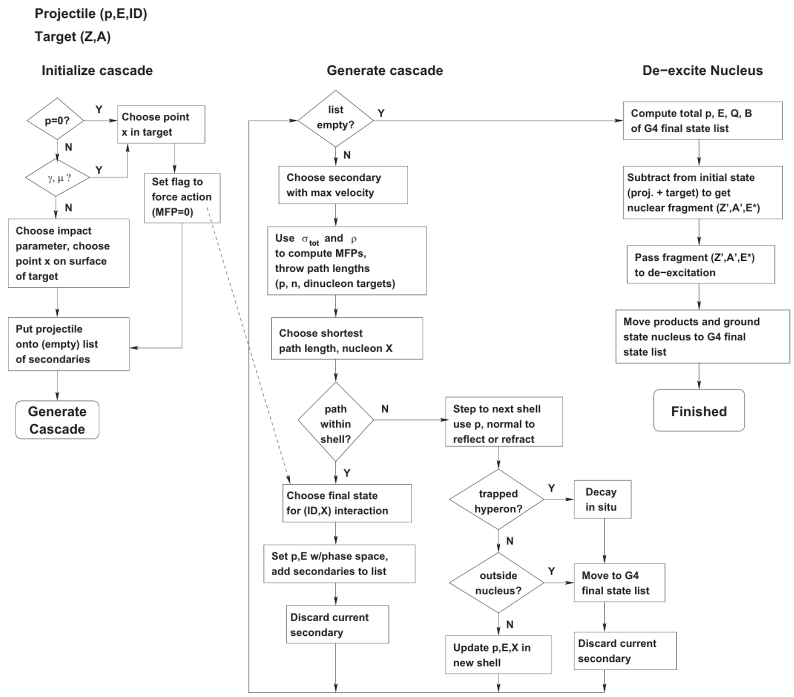

Figure 1.7: The general algorithm for a Bertini-style cascade. [16]

$$R_{max} = R_0 + 8a + \sqrt{\frac{\sigma_{tot}^{NN}}{\pi}} \tag{1.27}$$

where R_0 and a are the radius and diffuseness of the target nuclear density, respectively, and $\sigma^N N_{tot}$ is the total nucleon-nucleon cross section sampled at a given energy. The last term is particularly important for low energy interactions, where the interaction range may become very large due to the increasing cross section.

Nucleons in particular have isospin and energy-dependent potential wells. This dependence is taken from phenomenology of the real part of the optical model potential.

The end of an event simulation occurs when all participant particles exit the working sphere or the "stopping time" is reached. The simulation stopping time is determined within INCL itself. It is given by (parameterized in units of fm/c)

$$t_{stop} = 29.8 A_T^{0.16} \tag{1.28}$$

where A_T is the target mass number.

The Bertini and INCL models present two different ways of modeling and simulating some of the most complicated interactions found in hadronic systems. These differences, as we will see in chapter 3, are not large enough to provide significant deviations in our simulations from data, but they give us valuable insight into the inner workings of Geant4.

With neutron interactions sufficiently described in both reality and simulation, we will move to a detailed description of the detector and experimental setup for the SuperFGD neutron exposure tests.

Chapter 2

Experimental Setup

2.1 SuperFGD Concepts

The SuperFGD is one of many new detectors installed at ND280 to reach Phase II of T2K [19]. As discussed in the introduction, the previously used FGDs, plastic scintillating bar detectors, did not provide enough acceptance to limit systematic uncertainties to desired values. Specifically, the bars were aligned only in the x and y directions (with the beam traveling along the z direction), limiting the acceptance to only the forward direction. In order to further decrease systematic uncertainties, a larger angular acceptance was needed. Thus, the SuperFGD was proposed with three main design concepts:

- A sufficiently large mass to act as an active target for neutrino interactions,
- a high angular acceptance for charged leptons produced in charged current neutrino interactions, and
- the capability to reconstruct tracks of low energy hadrons around the neutrino interaction vertex.

Note that neutron detection capabilities are not among the main design goals for the SuperFGD. The fact that this capability is demonstrated was observed in initial tests for the detector. Once this property was found, though, it became of great interest to the collaboration. Recall that approximately 10% of the neutrino energy is carried away by neutrons in events which produce them. Therefore, this presented an opportunity to further decrease systematic uncertainties beyond what the SuperFGD already proposed to do.

The SuperFGD is a typical plastic scintillator detector. This means that its method for particle detection is absorption of ionizing radiation produced

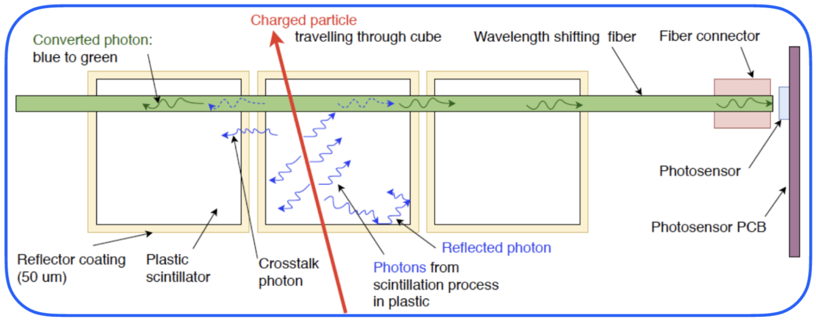

Figure 2.1: A diagram of scintillation light being produced and collected within a single cube of the SuperFGD. [21]

by charged particles moving through the detector medium, which in turn is emitted as scintillation light [20] [8]. As will be discussed later, the detector is constructed to keep scintillation light optically confined within a segment, where it can be collected by optical fibers. These fibers are "wavelength shifting", allowing us to bring the scintillation light to a wavelength optimized for signal recording. A diagram of this process is shown in Fig. 2.1. In the next few sections, we will go into more detail regarding the scintillation material and detection systematics.

2.2 The SuperFGD Prototype

The SuperFGD prototype [22] tested at LANL in 2019, originally built and tested at CERN, is comprised of 9,216 plastic scintillator cubes in an array of dimensions $24\times8\times48$ along the x, y and z dimensions, respectively. Each cube is $1\times1\times1$ cm^3. This size is motivated by the interaction length of a 200 MeV proton in plastic, a typical energy for protons produced in neutrino interactions at T2K. The cubes are covered in all sides in an optical reflector. Ultimately, the cubes are constructed to be as similar as possible to the cubes used in the actual SuperFGD. In order to achieve the 3D readout capabilities needed for granularity improvements over the original FGD, 3 orthogonal wavelength-shifting (WLS) fibers run through each cube to collect scintillation light. At the end of each fiber, a silicon photomultipler (SiPM), also referred to as a Multi-Pixel Photon Counter (MPPC), collects the light carried by the fiber to be sent to readout electronics and converted into electric signals.

The plastic composition of the cubes is polysterene doped with 1.5% paraterphynel (PTP) and 0.01% 1,4-bis benzene (POPOP). The PTP and POPOP dyes are used to bring the scintillation light closer to the maximum of the WLS

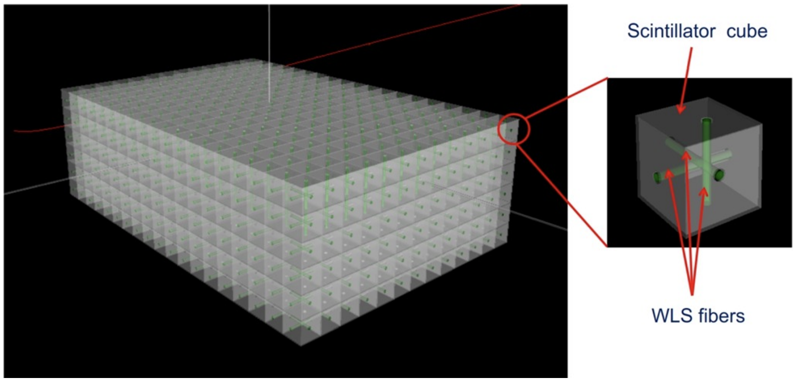

Figure 2.2: Diagram of the SuperFGD with a closeup of a single cube, showing the three orthogonal WLS fibers. [23]

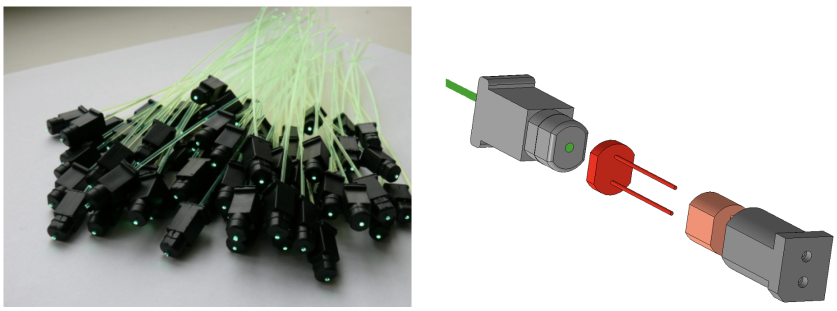

Figure 2.3: Left: WLS fibers with the custom plastic caps attached. Right: Diagram depicting the coupling interface between the WLS fiber (green) and an MPPC (red). A foam spring (orange) is used to ensure contact. [22]

fiber absorption spectrum. The optical reflector is white polystyrene, etched onto each of the cubes with a chemical agent, resulting in a coating 50-80 μm thick. Thus, the scintillation material and reflector are entirely composed of hydrocarbon.

The holes that contain the WLS fibers are 1.5 mm thick, with the fibers themselves 1 mm thick. The fibers used are the same as the WLS fibers in the FGD. Each fiber is connected to an MPPC container with a custom plastic cap originally developed for T2K's BabyMIND detector (Fig. 2.3).

Three types of MPPCs (Types I, II, and III) are employed by the SuperFGD prototype in order to test the effectiveness of two additional MPPC types compared to the model proposed for use in the SuperFGD (Type I).

The readout and event reconstruction method uses each plane (XY, XZ, YZ) of MPPCs seperately. Information from two of these readout planes can determine each event's position (with precision dictated by the cube size),

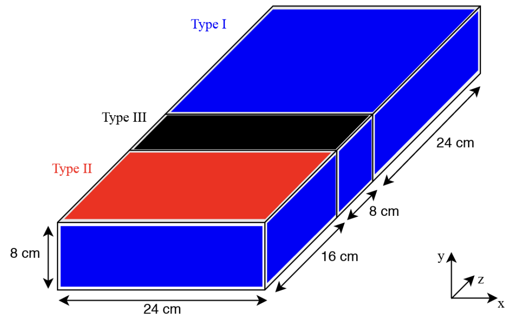

Figure 2.4: Distribution of the three types of MPPCs on the SuperFGD prototype. [22]

while the third plane's information is used to resolve any ambiguities in the particle track. The information from the three readout planes can be taken together to form a 3D view of each charged particle track.

2.3 CERN Beam Test

In 2018, the SuperFGD prototype was constructed and tested at CERN [22]. Here, it was exposed to a charged particle beam at CERN-PS T9 beamline. Time-of-flight counters were installed along the beamline to provide further particle identification. By setting the beamline magnets to predetermined values, particle momenta between 400 MeV and 8 GeV were chosen. The detector was tested in two beam modes: the "hadron" mode exposed the detector to protons, π^+, μ^+ and e^+ and the "muon" mode included beam stoppers to remove the hadronic part of the beam along with most e^+. Additional modifications could be made to the beamline to change the relative fraction of projectiles when running in "hadron" mode.

Many elements of the detector response were studied in this test. The relevant quantities studied are hit amplitude thresholds, the hit time structure, optical crosstalk between cubes, channel response, and light attenuation through the WLS fibers.

We will now briefly outline the reported measurements of the detector response. For the following results, note that there are three signal outputs providing information for an event. "High gain" (HG) and "low gain" (LG) signals are extracted through peak detection in the analog signal, which "time over threshold" (ToT) signals are calculated by taking the difference between falling and rising edge timestamps in a signal. ToT allows us to register hits that would otherwise not be recorded by the other two signal paths.

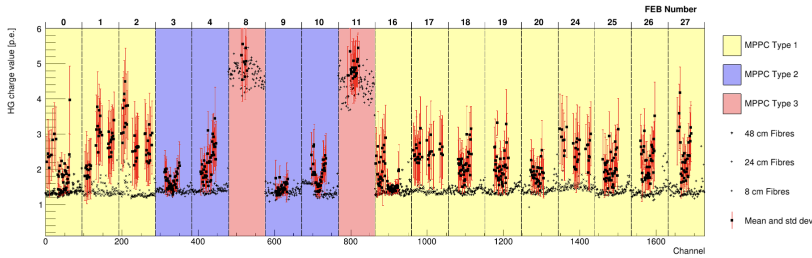

Figure 2.5: Measured values of the hit amplitude thresholds for each readout channel. Black squares represent the mean value for the minimum high gain (HG) readouts for each channel. [22]

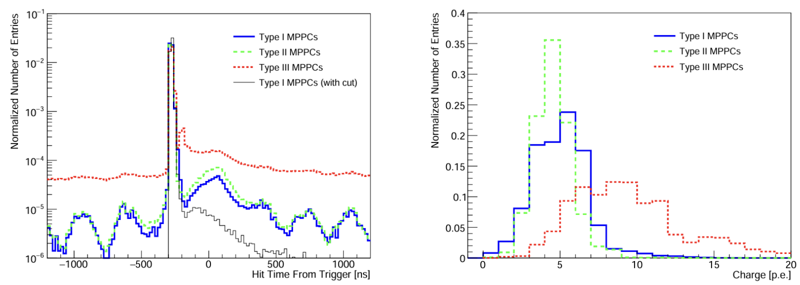

Figure 2.6: Left: Time structure of an event around an external trigger at -250 ns for the three MPPC types, as well as for MPPC type I with a timing cut eliminating the beam structure. Right: Average charge recorded in the time windows of interest. [22]

The hit amplitude thresholds, measured in photoelectrons (p.e.) can be seen in Fig. 2.5. These thresholds set a minimum value for the light yield that can be measured by each readout channel. Of particular note is the response differences between the different MPPC types.

The time structure for a single hit is shown in Fig. 2.6. This result was recorded with a muon beam with momentum 2 GeV. The repeating structure seen in the left side of Fig. 2.6 is a substructure of the proton beam, specifically the PS accelerator's revolution frequency of 477 kHz. The time structure can be used to estimate a "recovery time" before a channel is ready to receive information from a second hit. Since the main peak around the triggered event has a width of about 100 ns, this recovery time is estimated to be on the order of 200 ns.

The channel response was studied in order to understand detector uniformity. Some measurements of channel response are shown in Fig. 2.7. Note the discrete nature of the ToT signal. This is due to the sampling rate for this

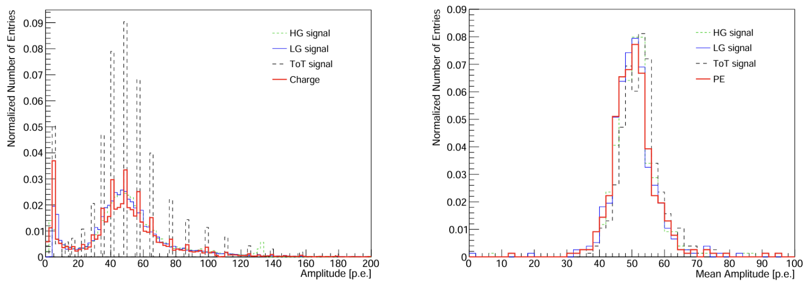

Figure 2.7: Left: Response of a readout channel to a minimum ionizing particle along a 24 cm fiber connected to a Type I MPPC. Right: Mean light yield for 384 channels along 24 cm fibers connected to Type I MPPCs. Both plots show results for each signal processing path. [22]

measurement, which has a 2.5 ns resolution. Importantly, the distributions on the right plot of Fig. 2.7 show a similar mean and standard deviation. This is an indication that the calibration parameters were correctly applied to each signal path.

Optical crosstalk was studied in depth in order to eliminate possible ambiguities in event reconstruction–if crosstalk is high, then the fine granularity of the detector can become significantly smeared. Crosstalk occurs when scintillation light produced in a certain cube travels to a neighboring cube. An illustration of this effect is shown in Fig. 2.8. In anticipation of this effect, a layer of Tyvek light insulator was placed in between each layer of x-z cubes, resulting in asymmetric crosstalk measurements in the x and y directions. The measurements are shown in Fig. 2.9. The crosstalk percentage κ (percentage of light that flows from main cubes to neighboring cubes) is given by

$$\kappa = \frac{M_{xtalk}}{M_{main} + 2M_{xtalk}} \tag{2.1}$$

where M is the light measurement collected by the relevant cubes. The extra factor of $2M_{xtalk}$ is included since crosstalk light is recovered two times from the contributions of the main cube's neighbors.

Light attenuation in the WLS was studied and calculated. Photon attenuation is a well-known effect and is modeled by the equation

$$y(d) = LY_0(\alpha e^{\frac{-d}{L_S}} + (1-\alpha)e^{\frac{-d}{L_L}}) \tag{2.2}$$

where LY_0 is the unattenuated light yield, α is a weighting factor, L_S and L_L are short and long attenuation constants, respectively, and d is the distance from the center of the cube with the main energy deposit to the

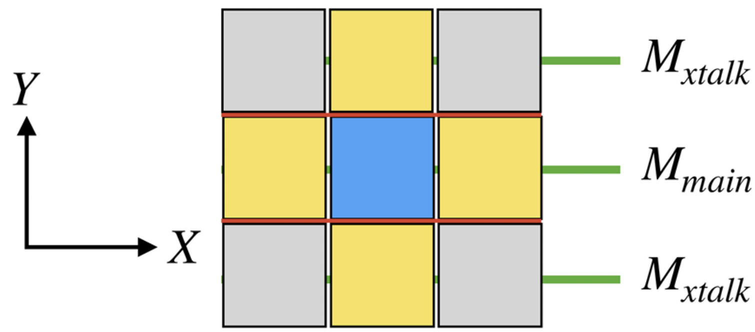

Figure 2.8: Sketch of the main cube (blue) and possible crosstalk cubes (yellow) for a certain hit in the x-y plane. Fibers are shown only in the x direction. [22]

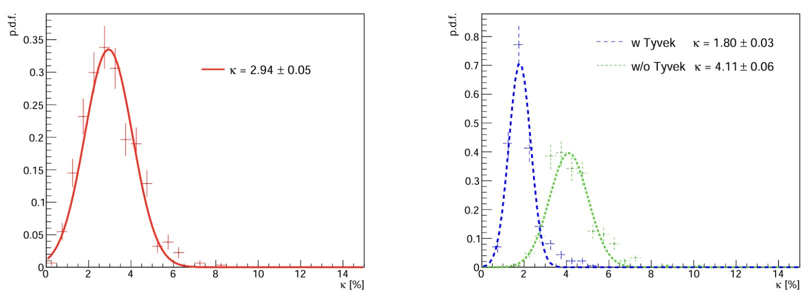

Figure 2.9: Left: Crosstalk percentage κ between cubes in the x direction. Right: κ measured between cubes in the y direction with and without light insulating Tyvek. [22]

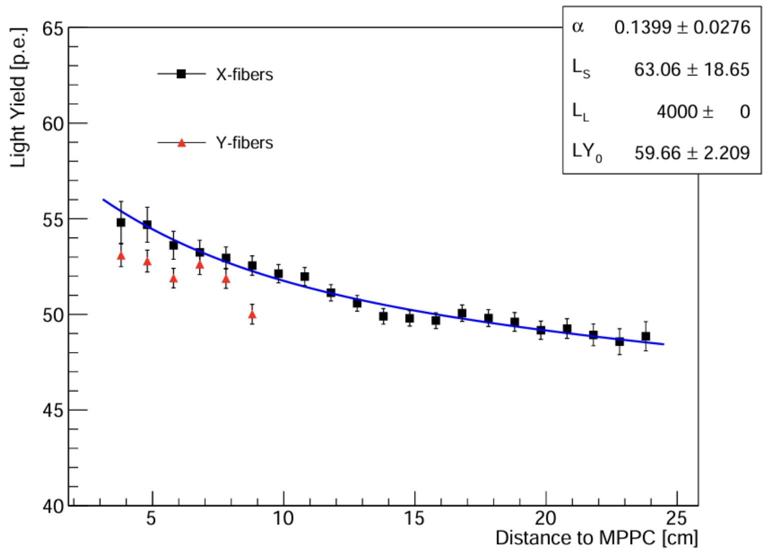

Figure 2.10: Light attenuation in 8 cm and 24 cm long fibers. The solid line is the fit of Eq. (2.2) to the 24 cm fiber attenuation points. [22]

MPPC detecting the signal (including a 2.3 mm offset). L_L is given by the manufacturer as 4 m, while L_S depends on the specific length of the fiber. The attenuation in the x and y direction (24 cm and 8 cm fibers, respectively) is shown in Fig. 2.10 along with the measurements of the constants α and L_S. This measurement was performed by averaging the data of all channels in the x-z (y-z) plane for each specific y (x) distance.

Finally, time resolution has been studied extensively [24]. Good time resolution is critical for making a time-of-flight measurement of neutron energies. As seen in Fig. 2.13, the sampling rate of the electronics used to convert analog to digital signals in the SuperFGD prototype is 2.5 ns. Thus, the time resolution of a single channel cannot be less than $2.5/\sqrt{12}$ ns–the standard deviation of a uniform distribution within a 2.5 ns bin.

Many effects contribute to delays in detecting light produced in an event versus the actual production time. Such effects include re-absorption/emission of scintillation light by the PTP and POPOP dyes; time shifts in the arrival of the first photoelectrons decrease with an increasing amount of scintillation photons produced. Therefore, the time resolution improves with increased signal amplitude, as seen in Fig. 2.11.

The time resolution for a single channel was also studied. We will skip the details of the various methods used in this study for the sake of brevity and report the final result of $\sigma_{t_1} = 0.97$ ns.

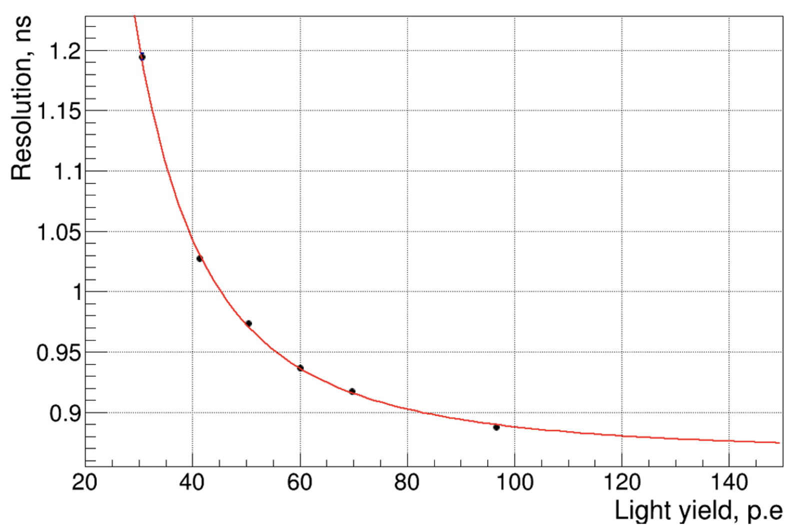

Figure 2.11: Time resolution dependence on the light yield for a single hit. [24]

Ultimately, the CERN beam test confirmed the feasibility of SuperFGD's construction as well as testing the main design goals of the SuperFGD. For the purpose of this work, it provided necessary calibration, resolution, and attenuation data to be used in the LANL beam test.

2.4 The LANL Neutron Beam Test

In 2019, the SuperFGD prototype was exposed to a spallation-produced beam of neutrons with energies 0-800 MeV from Los Alamos National Laboratory's (LANL) Weapons Neutron Research (WNR) facility [23]. The detector was aligned such that its longest dimension (z) is parallel to the neutron beam. The beamline setup is depicted in Fig. 2.12. As shown, a proton beam impinges on a tungsten target with a predetermined pulse structure: Macropulses of 675 μs are sent with a delay of 8.33 ms. Each macropulse contains micropulses separated by 1.8 μs, with 7×10^6 protons per micropulse. All charged particles resulting from the proton-tungsten interaction are deflected by the upstream magnets so that only neutrons and photons arrive at the detector (all other neutral particles will decay before reaching the detector). Before their arrival, the beam is collimated twice to shape its profile and provide a narrow neutron beam compatible with the simple expression for neutron attenuation outlined in Eq. (1.6).

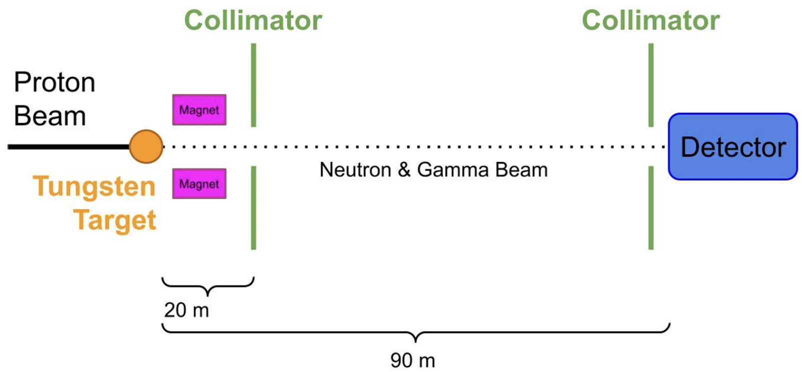

Figure 2.12: LANL WNR beamline setup. [23]

The photons will always arrive at the detector before the neutrons, producing a sharp peak (the "gamma flash") followed by a broader signal curve as the neutrons arrive, as seen in Fig. 2.13. By measuring the neutron time of arrival relative to the gamma flash, we can find the neutron energy through the time-of-flight (ToF) technique. In the real SuperFGD, the time-of-flight is measured between a neutrino vertex (identifiable from the resultant emitted lepton) and the neutron vertex, measured as the earliest energy deposition by secondary particles at a point removed from the neutrino vertex. This method of indirect neutron detection is sketched in Fig. 2.14.

Since the detector is of appreciable distance (90 meters) from the neutron source, neutrons of different energies are more separated in their arrival. This is a double-edged sword: we improve our resolution from high energy neutrons, but low energy neutrons may be slow enough to interfere with the gamma flash and high energy neutron signal from the next micropulse. Thus, a cut of 13 MeV is placed on the neutron energy to eliminate this interference effect.

Having now described many details of neutron interactions, how these interactions are simulated in Geant4, and the experimental setup for the SuperFGD prototype tests, we can move on to further discussions of specific analyses performed on simulations of the SuperFGD prototype.

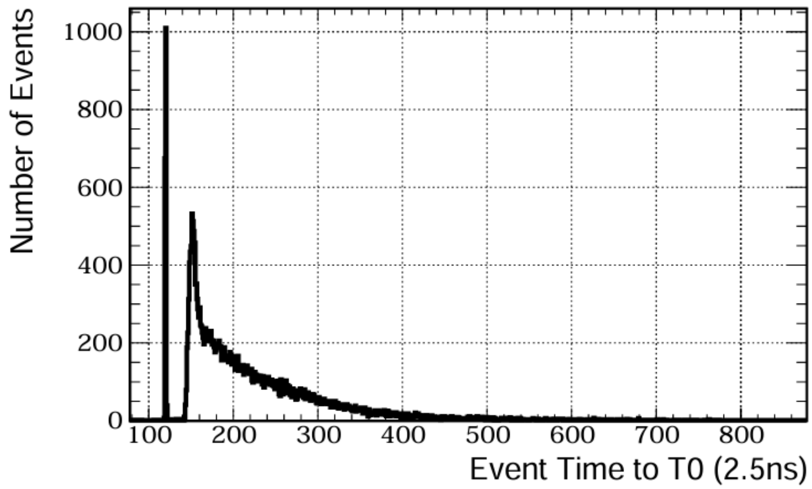

Figure 2.13: Time distribution of an event relative to T_0, the time of proton interaction with the tungsten target. Both the gamma flash and subsequent neutron signal are visible. This figure is binned in 2.5 ns bins, the sampling rate of the readout electronics. [23]

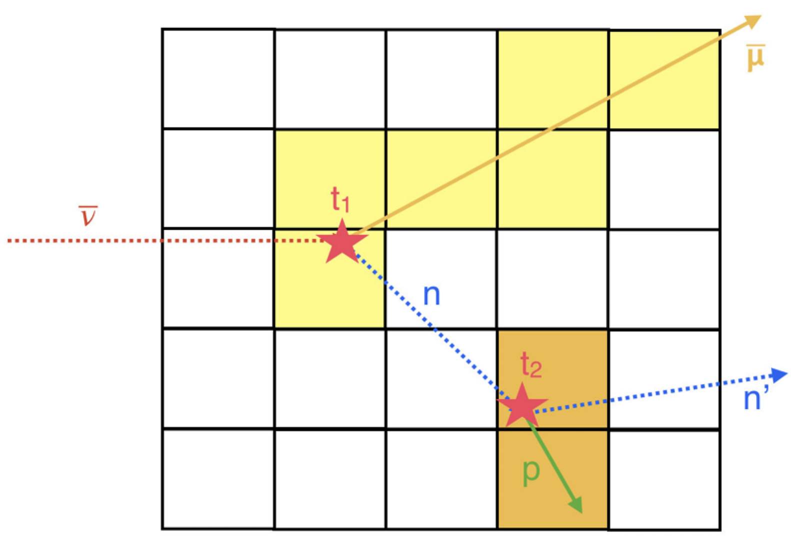

Figure 2.14: Sketch of indirect neutron detection from an antineutrino interaction. Each cube represents a voxel in the detector. The times t_1 and t_2 are measured to infer the neutron time-of-flight. [25]

Chapter 3

Monte Carlo Simulation and Analysis

3.1 Monte Carlo Simulation Chain

In chapter 1 we have outlined the various ways in which neutron interactions can proceed (reword this), taking into account both the physical interactions of the neutron and the way in which these particles are handled in Geant4. Then, in chapter 2, we discussed the physical specifics of the SuperFGD prototype and how data is collected with the detector. Now, we turn to a description of the Monte Carlo simulation process and the way that the simulation is analyzed, eventually concluding with comparisons between these simulations and data.

The event simulation is handled by a package named Edep-Sim [26], a Geant4 wrapper which allows the user to easily upload geometry files, handle particle gun configuration, and record truth variables in a ROOT file.

With a complete simulation file, we can move into the LANL-specific codebase. We take all the values from the simulation file and use a relatively simple Python program to format them into a ROOT tree. Specifically, this program takes the particle's kinematic attributes at each point along each trajectory for each event that was simulated. In theory, we can store any attribute that Geant4 has access to in the output of this program. For this work, the most useful of these extra attributes are particle type and process type (i.e. elastic or inelastic interaction) in addition to the kinematic variables mentioned before. However, this step of outputting all of our desired variables does not result in a fully structured file ready for analysis.

Now with a ROOT file containing all of our desired variables, we must apply detector effects to the "true" tracks in order to obtain a result that is consistent with data. The script that handles this applies many uncertainties using values that were recorded in the CERN beam test. The most important examples are light yield uncertainties (i.e. errors associated with the conversion of deposited energy to a photoelectron count) and attenuation uncertainties (i.e. errors associated with the propagation of light from the voxel to the MPPC). Thus, the output file of this script resembles a typical data file and it is therefore ready to proceed to selection and analysis.

3.2 Single-track Event Selection

Before proceeding to a description of the analysis, it is important to recall the specific make of the SuperFGD prototype: It is a scintillation detector consisting of nearly 10,000 cubes/voxels of equal size (1 cm x 1 cm x 1 cm). The reconstruction algorithm used in the LANL software makes full use of this–it is designed to determine which voxel the scintillation light we observe originated in. This gives a clear definition of our possible selection accuracy, since we obviously cannot measure the position of a particle in the SuperFGD to a finer degree than the size of the voxels within the detector. This gives the SuperFGD a nominal spatial resolution of ≈ 0.29 cm, given by the fact that the standard deviation of a continuous uniform variable between 0 and 1 is $1/\sqrt{12}$. Additionally, the complete 3D granularity of the detector allows the reconstruction algorithm to produce tracks for charged particles (recall that non-charged particles will not produce scintillation light and therefore will not leave a track within the detector) which can be visualized if desired. With this in mind, we can define our desired signal for studying neutron interactions, a so-called single-track event. The easiest way for us to identify a neutron interaction vertex is to have 1 charged particle in the final state–thus, a single-track event will only leave one track in the detector. Since the incoming neutron does not produce a track, observing a single-track event allows us to find the interaction point as the beginning of the charged track we observe.

The selection script applies cuts to each event in order to maximize the amount of single-track events we find:

- Photoelectron cut: Any hit must produce greater than some amount of photoelectrons to be considered.
- Single cluster cut: Require that we reconstruct only a single track in the detector in order to put a strict definition on our topology.
- Voxel cut: Each track must have at least 3 voxels within it. This cut along with the photoelectron cut reduce noise from low energy parti-

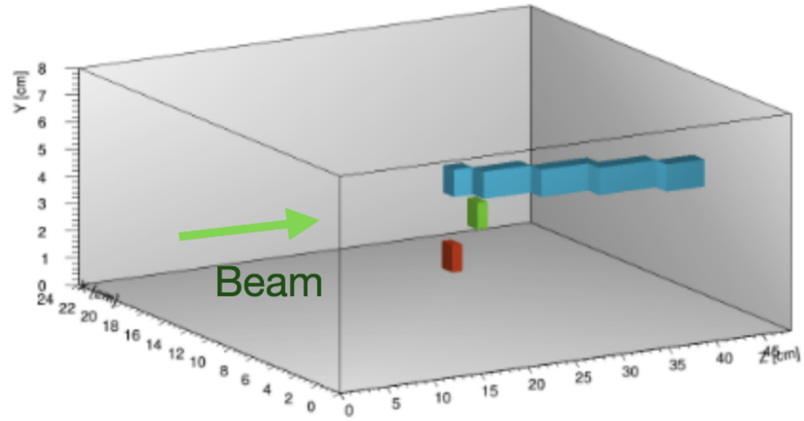

Figure 3.1: A view of three different clusters in a single event, tracked in the SuperFGD after the voxelization algorithm is applied. Different colors mean that distinct clusters were identified. [21]

cles, either from neutron/secondary interactions or cosmic rays if we are analyzing data.

- Fiducial volume cut: Each track must be contained within the fiducial volume of the detector. This cut allows us to disregard tracks that are not fully contained and therefore may provide incorrect information towards the analysis.

- Principal vector cuts: We define a set of tracks coming from a single vertex to be a cluster. By diagonalizing the covariance matrix associated with a cluster, we can define the principal vector as the eigenvector with the highest eigenvalue. This matrix is defined by

$$M_{ij} = \sum_{i,j} \frac{(\boldsymbol{v} - \boldsymbol{c})_i (\boldsymbol{v} - \boldsymbol{c})_j}{N} \tag{3.1}$$

  where $\boldsymbol{v}$ is the position of a voxel in the identified cluster and $\boldsymbol{c}$ is the center of the cluster. By requiring that the principal vector is large and that the next largest eigenvector is small, we can assure that we keep only long, thin clusters that are likely to be associated with a single track.

  These cuts are further delineated into three types. First, the linearity cut requires that $(\lambda_1 - \lambda_2)/\lambda_1$ is greater than 0.7, where λ_i is the ith eigenvalue. This rejects "blob-like" clusters. Next, the cluster width cut

Figure 3.2: An illustration of two clusters and their estimated "cluster width". $\boldsymbol{e_2}$ represents the second eigenvector of the principal cluster matrix. [21]

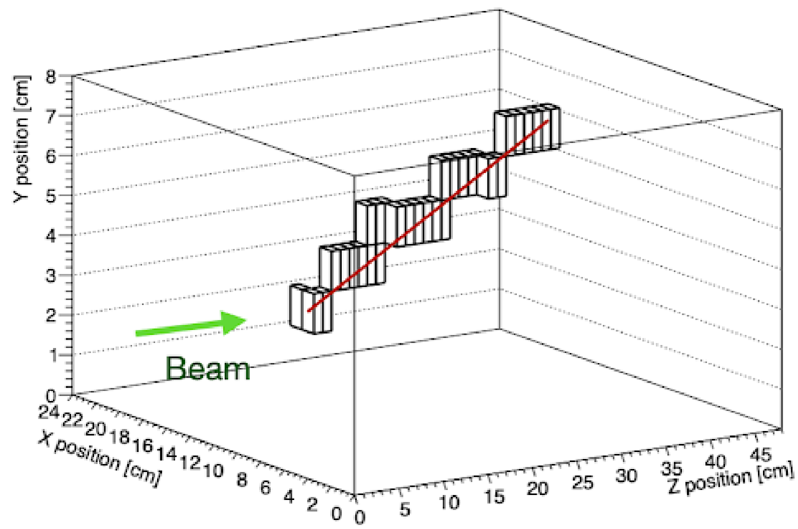

Figure 3.3: A single-track event readout of a cluster with its best fit line projected on top of it. [21]

chooses thin clusters. This is done by projecting the distance between each voxel and the center of the cluster along the second eigenvector and requiring that the two voxels furthest from each other are not more than 1.4 cm apart (see Fig. 3.2). Finally, the line-voxel max distance cut (referred to hereafter as the "max vox line" cut), rejects events with a separation between voxels and the best fit line (see Fig. 3.3) greater than 1.2 cm.

Once the single-track selection is finished, the program can record kinematic variables and, more importantly, the layer in which an interaction occurred. We can use this information to build the neutron interaction cross-section.

We use the so-called "extinction method" to extract the cross section. This principle revolves around the neutron attenuation equation (Eq. (1.6)) introduced prior:

$$N(z) = N_0 e^{-\lambda z} \tag{3.2}$$

Where z indicates the interaction layer (we define the neutrons to fly along the z axis), N_0 is the initial number of neutrons, and λ is an extinction parameter equal to the hydrocarbon density ρ times the cross-section σ. Thus, by fitting the interaction layer distribution from our selection script with this exponential, we can easily extract λ and the cross-section. Note that solving this equation for σ gives us a method of "direct extraction":

$$\sigma = \frac{\ln\left(\frac{N_0}{N_0 - N(z)}\right)}{\rho z} \tag{3.3}$$

This equation can be useful as a second check of cross-section values at a particular energy.

3.3 Monte Carlo Studies

With the specifics of our simulation and analysis chain laid out, we can move on to a discussion of how to study the analysis process to best match our simulation results to reality. The parameters of the analysis scripts that apply detector effects and single-track event selection cuts can be freely changed. For example, we may normalize the effect of the three different MPPC types used in the detector, i.e., make all the MPPCs have the same response as type I MPPCs. We may adjust the values of our selection cuts or remove them entirely, as seen in Fig. 3.4. We can thus study the response of our event sample to either minor or major changes in our analysis procedure. This can be useful in determining which of our cuts is most limiting to our sample or in trying to determine the overall behavior of neutrons in the detector. Note that all figures present in this section are results for the Bertini physics list. The following tests were also performed with the INCL physics list, but these results are excluded from this section for the sake of brevity.

One of the most important quantities we can compute is the analysis' selection efficiency. We define this to be the number of events that pass our selection cuts divided by the total number of events that were simulated. This quantity can tell us how many events we must simulate in order to get a sample statistically significant enough to compare with data. We can simply check the number of events remaining after each cut is applied to see how our selection process affects the selection efficiency. An early result of this calculation is shown in Fig. 3.5.

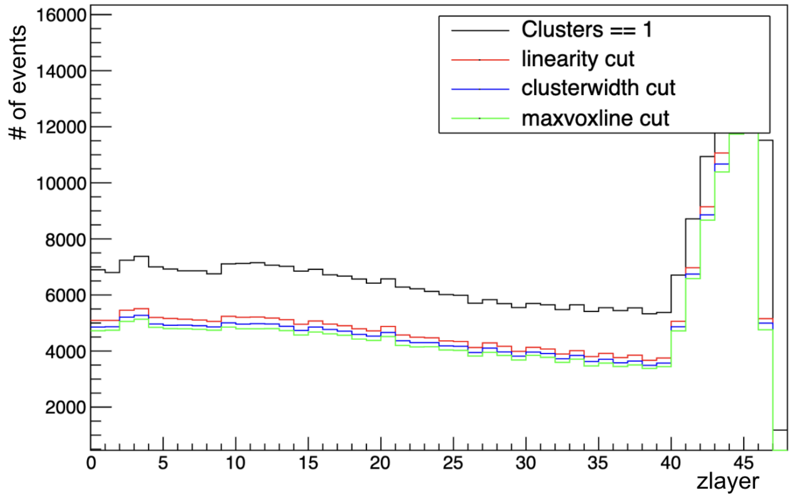

Figure 3.4: The distribution of neutron interaction vertices along the z layer of the detector with the principal vector cuts removed then reapplied one at a time. Layers 40-48 are not considered in our cross-section fit due to end-of-detector effects.

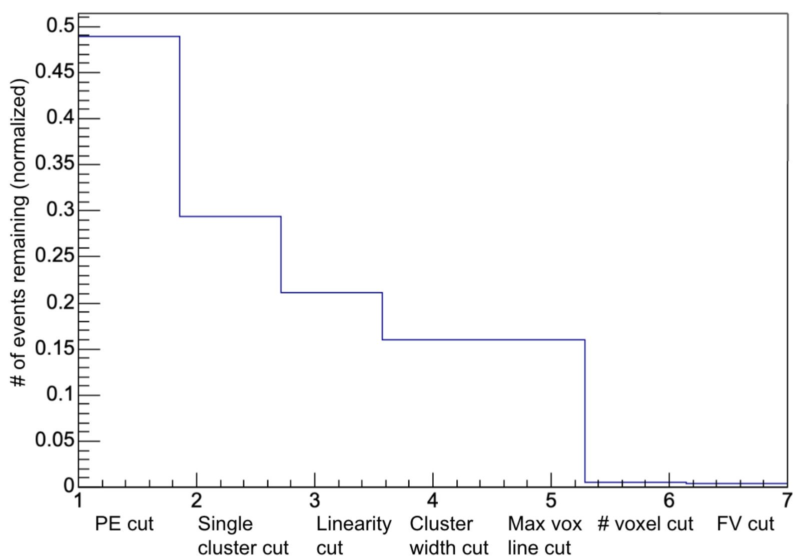

Figure 3.5: Selection efficiency for each cut applied in our analysis.

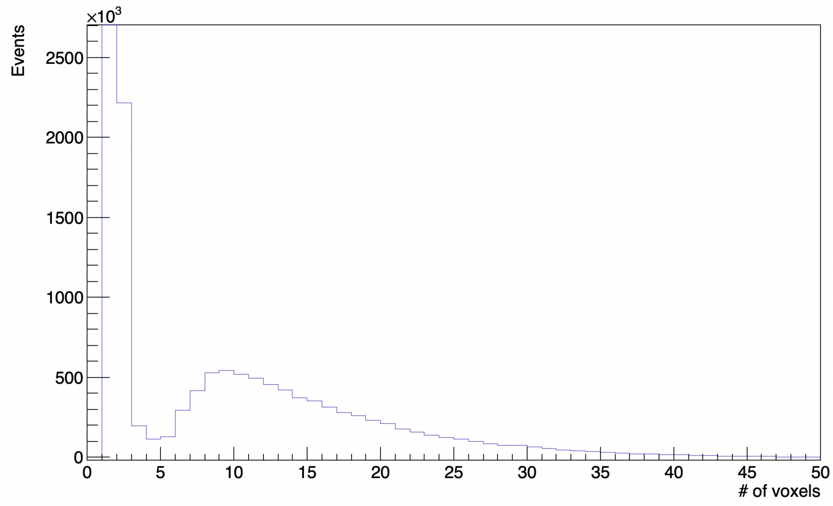

Figure 3.6: Event count vs. the number of voxels in their reconstructed track. A significant amount of events are reconstructed with 1 or 2 voxels, so the plot is slightly zoomed to show detail for events with a number of voxels greater than 2.

From Fig. 3.5, it is clear that the cut on the number of voxels, as it was initially applied, is extremely restrictive. The initial application of this cut was to only include events with a number of voxels between 3 and 8. This restriction resulted in a selection efficiency of less than 1% after all cuts were applied. So, in order to maintain a statistically significant sample without requiring a massive amount of events to be simulated, this cut underwent significant changes. First, it is informative to see exactly how many events this cut is excluding in its initial form. A plot of the number of voxels for a typical simulation is shown in Fig. 3.6. This plot shows that there are many events with greater than 8 voxels that are completely removed by the initial form of the cut.

To encompass all events with our chosen topology, we would like to keep all of these events, so long as the reconstructed track is entirely contained within the detector. The form of this ”containment” cut is relatively simple: by setting the maximum number of voxels in a track to 48 (the last layer of the detector) minus the layer of interaction for a specific event, we can guarantee that all of the selected events will be contained. We can impose an additional restriction: by skipping events that have an interaction vertex at a layer greater than 40 (the end of our extinction method fit), we can avoid end-of-detector effects, which may contaminate our topology.

Recalculating the selection efficiency with this new version of the cut, we

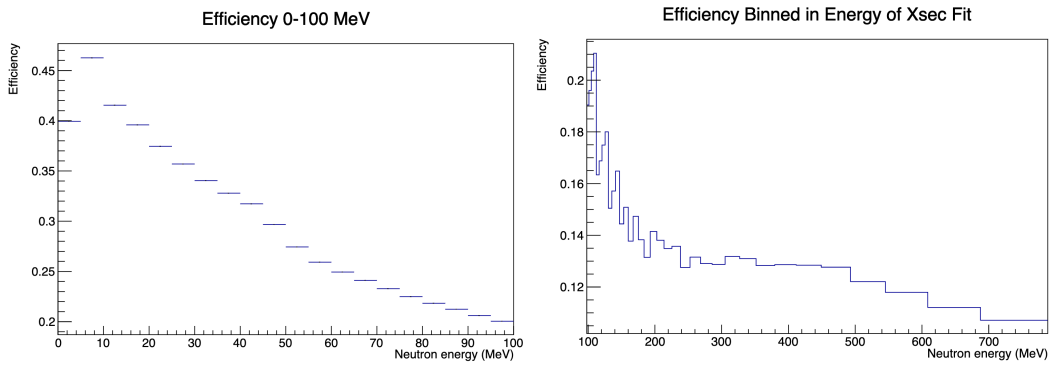

Figure 3.7: Selection efficiency with improved containment cut. Left: Selection efficiency for energies 0-100 MeV. Right: Selection efficiency for energies 100-800 MeV, using the binning of the cross-section fit.

find that it has improved drastically. Fig. 3.7 shows a selection efficiency of 50% for low energy neutrons, plateauing around 10% as we move to higher energies.

This cut certainly results in a statistical improvement over its prior implementation, but spurious "low voxel" events still appear in our selection–including the minimum voxel cut with the upper containment cut produces unexpected and unphysical results in the cross section measurement, so we cannot use that bound in general. This is due to a "pile-up" effect in the interaction layer distribution caused by the combination of a running maximum voxel cut with a fixed minimum voxel cut–this effect distorts the distribution out of its expected exponential shape and invalidates the extinction method we use to fit the cross section.

Let us now look at the angular distribution of events–this variable together with voxel number gives us insight into charged particle trajectories through the detector. We can calculate the angle that a reconstructed event makes with the z axis. To do so, we can use the principal vector we already calculated for the associated cuts:

$$\theta = \arctan \frac{\sqrt{\boldsymbol{p}_x^2 + \boldsymbol{p}_y^2}}{\boldsymbol{p}_z} \tag{3.4}$$

We find that there is a tendency in our reconstruction algorithm to assign an event a 90-degree angle ($\cos(\theta) = 0$) no matter the true angle. This and other degeneracies can be seen in Fig. 3.8.

While our ability to study our reconstruction algorithm is important, remember that this process is still subject to the detector's systematics. Specif-

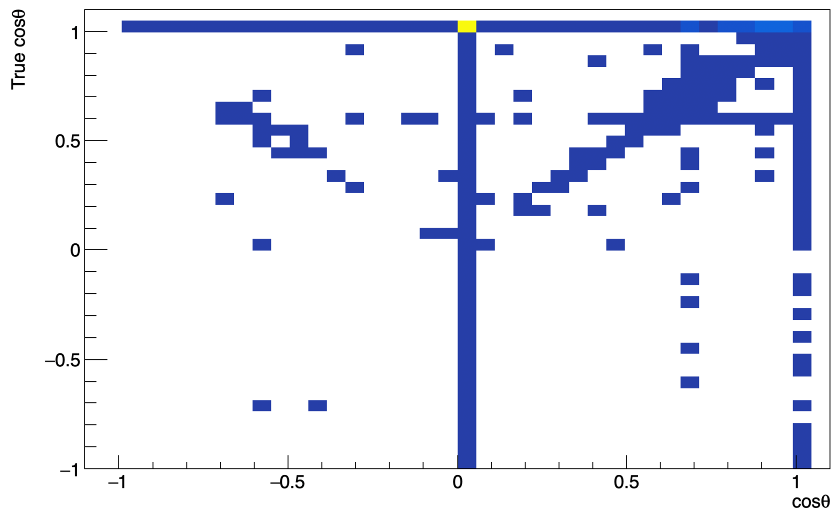

Figure 3.8: True vs. reconstructed $\cos(\theta)$. Note the degeneracies along reco $\cos(\theta) = 0$, true $\cos(\theta) = 1$, and across the $\cos(\theta) = 0$ axis–some events with a positive $\cos(\theta)$ may be reconstructed as negative.

ically, we must consider spatial resolution. Consider, for example, a track created at a sufficiently high angle such that its reconstruction is contained only within the x-y plane. This could result from an interaction taking place at the beginning of a cube in the z direction, traveling 3 or 4 voxels in the y direction towards the edge of the detector, then exiting the detector at the end of the top cube's span in the z direction. In the most extreme case, the track would have a true angle of $\arccos(\frac{1}{3}) \approx 70°$, but be reconstructed with an angle of $90°$. At its widest, in the x direction, a track may travel through 6 voxels without moving in the z direction. Thus we may make an alternative type of cut to the $\cos(\theta)$ cut described in the above paragraph. By requiring that the number of voxels in an event is greater than 6, we can rid ourselves of these events contained entirely within the x-y plane. However, further studies revealed that although this cut is theoretically sound, it suffices in most cases to only cut on 3 voxels in an event. These cuts and there effects are shown in Fig. 3.9 and Fig. 3.10. Since the number of events in the range of 3 to 6 voxels is low, demonstrated in Fig. 3.6, there is little statistical difference when distinguishing between the two additional cuts. It will be important to distinguish them when comparing to data, but for now we have demonstrated that we can remove events from the angular distribution that our algorithm struggles to reconstruct.

With sufficient studies performed to refine our event selection process, we can move to comparing the results of our simulation to data.

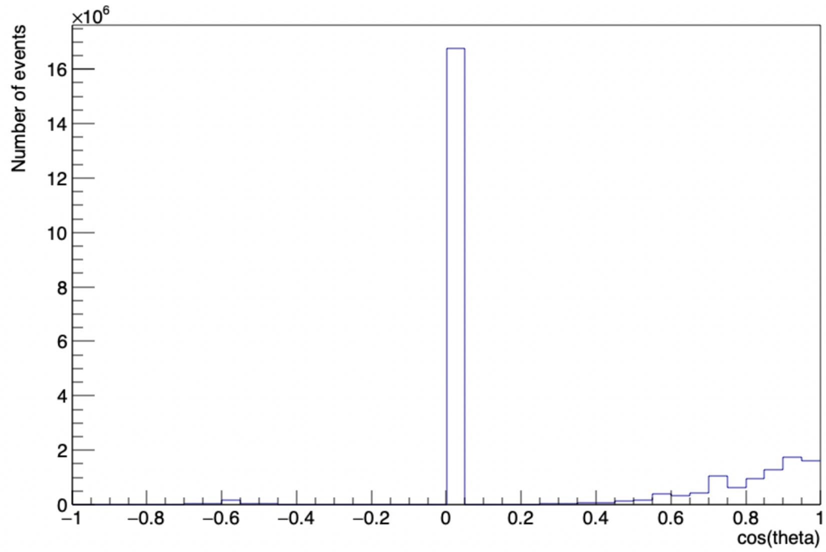

Figure 3.9: $\cos(\theta)$ distribution after selection with no additional cuts applied. Note the excess of events at $\cos(\theta) = 0$.

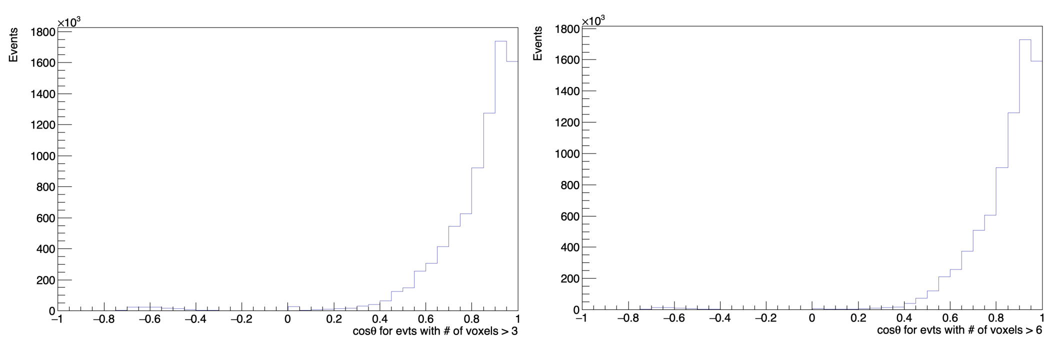

Figure 3.10: Left: $\cos(\theta)$ distribution after selection with an additional cut for number of voxels > 3. Right: $\cos(\theta)$ distribution after selection with an additional cut for number of voxels > 6.

3.4 Comparison between Simulation and Data

Before moving into variable distributions found in data, we present a short discussion on systematic uncertainties measured with data. We define the fractional uncertainty δ to be

$$\delta = \frac{N_0 - N_{180}}{N_0} \tag{3.5}$$

where N_0 and N_{180} are the number of events measured in data with the detector in a 0 degree or 180 degree rotation configuration respectively. Multiplying δ by the number of events measured in data for any particular distribution will give the systematic uncertainty for that measurement. By combining this with a $\sqrt{n}$ statistical uncertainty, we can report data measurements with relevant errors.

Since we have just discussed this topic in the previous section, we will begin by comparing the $\cos(\theta)$ distributions of our simulation to data. It is important to understand whether Geant4 can replicate trajectories of particles in our detector that we might expect to see. As seen in Fig. 3.11, the event rate in each bin of $\cos(\theta)$ is similar across both physics lists and data when put on the same scale. With a cut on the number of voxels at 3, though, our simulation tends to reconstruct more events with high $\cos(\theta)$ values. For the purposes of this study, this discrepancy is small enough that, when combined with the fact that it is rectified when the voxel cut is increased, we are confident that our tuned analysis procedure can handle particle trajectories from MC and data similarly.

After investigating the $\cos(\theta)$ distributions for MC and data, the natural next variable to consider is the number of voxels in an event. With these two variables together, we can get an idea of the trajectory for charged particles created from neutron interactions. This result is shown in Fig. 3.12.

This plot shows a striking feature: our simulations vastly overestimate the amount of events with a large number of voxels. In fact, the bin with the maximum amount of events for the data (number of voxels = 4) is a local minimum for the simulations. This results warrants further study that unfortunately was not done for this work–the cause for this discrepancy is unknown.

Now, we can present comparisons of the neutron interaction cross section measurement between simulation and data. Recall that we use the "extinction method" to extract the cross section, given by Eq. (3.2) and the relevant discussion. Recall additionally that inclusion of a lower bound on the number of voxels gives an unexpected result inconsistent with this method of calculation. In order to rid ourselves of the anomalous effects caused by the inclusion of

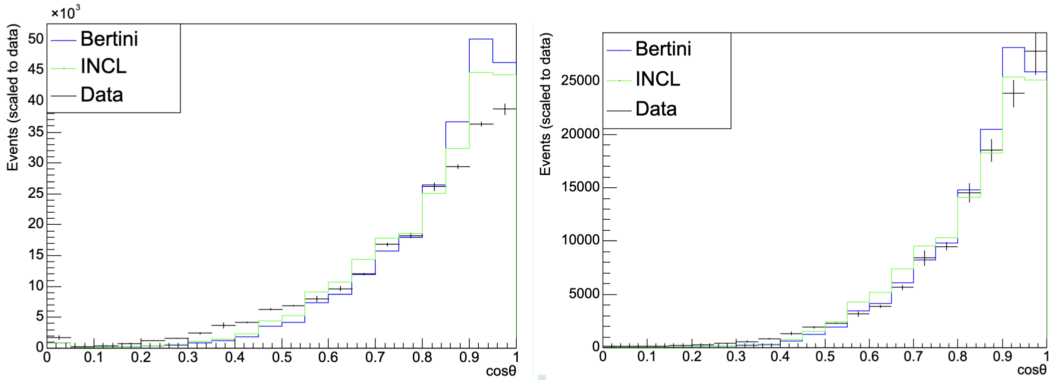

Figure 3.11: Comparison of $\cos(\theta)$ distributions for the Bertini and INCL physics lists to data. The number of events for each simulation has been scaled to data. Left: Additional cut for number of voxels > 3. Right: Additional cut for number of voxels > 6.

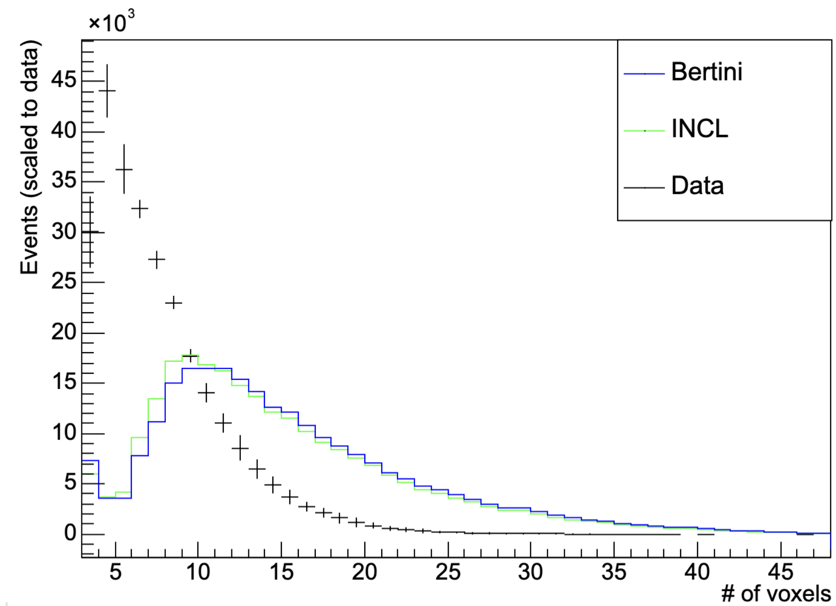

Figure 3.12: Voxel number distributions for the Bertini and INCL physics lists along with data. Again, the number of events in each simulation has been scaled to the data.

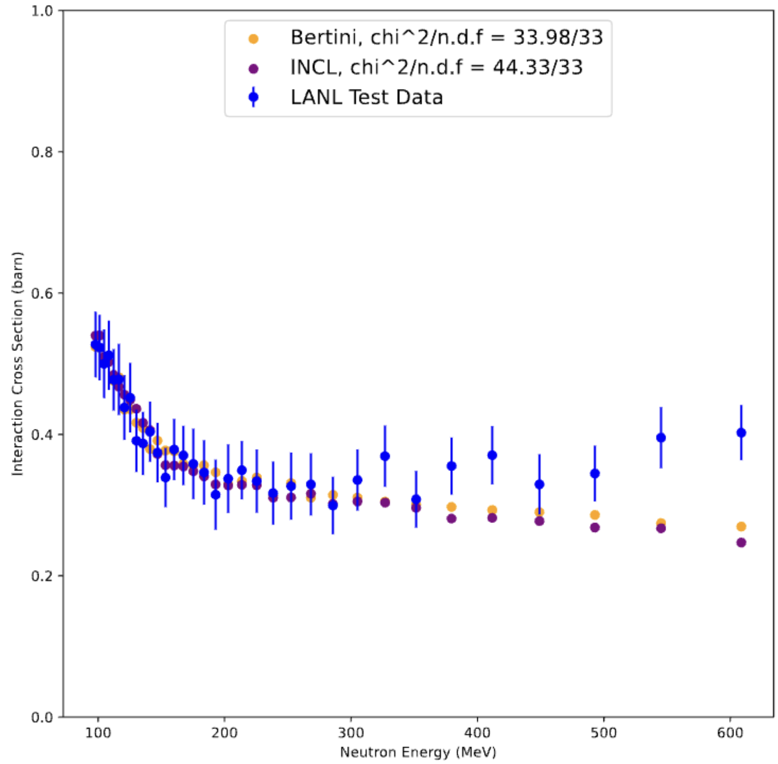

Figure 3.13: Neutron interaction cross sections measured with the Bertini and INCL physics lists and compared to data taken in 2019 and published in 2023. [23]

low voxel events, we implement a secondary containment cut. This cut is used only for the cross section measurement and limits the range of the detector that we consider for the fit to only the first 20 layers. As of now, this cut is empirical–further study is required to develop a cut that is consistent with our understanding of the measured kinematic variable distribution. The cross section fits we obtain are presented in Fig. 3.13.

The Monte Carlo simulations show fair agreement with the data overall; the agreement is exceptional for kinetic energies less than 300 MeV, but diverges slightly as the neutron kinetic energy increases. Recall, however, that the peak of T2K's neutrino energy distribution is near 600 MeV. Thus, CCQE interactions which produce neutrons (and thus must also produce leptons, typically muons) limit the neutron kinetic greatly, landing the expected neutron kinetic energy distribution within the range of agreement between our fits and data.

Conclusion

In pursuit of the goal of investigating Geant4 simulations, how they model neutron interactions, and comparison of these simulations to data taken at the 2019 LANL beam test of the SuperFGD prototype, we have discussed many topics. In chapter 1, we laid out the basic theory of neutron interactions, with particular focus on the cross-section and hydrocarbon interactions, along with an overview of Geant4 and its capabilities in the context of hadronic physics. In chapter 2, we took an in-depth look at the SuperFGD prototype. We discussed its conceptual design as well as all of the systematics present in the CERN and LANL beam tests. In chapter 3, we described the Monte Carlo simulation chain, the event selection and analysis procedure, some studies performed on simulations to refine the analysis, and finally compared select results to data taken in 2019.

This work represents a large undertaking into understanding the simulation models used in the T2K experiment, specifically for the study of neutron kinematics. It stands as a compilation of information regarding neutron interactions in intermediate energy ranges; many sources in nuclear physics are not concerned with hadronic interactions above 20 MeV, while many high energy physics sources are only comprehensive for energies larger than 1 GeV. By providing a comprehensive review of theoretical and experimental inputs to Geant4 in energy ranges and modes previously underrepresented in literature, we hope to create a solid foundation for future work in this area. We have made significant strides towards understanding limitations in the simulation chain. Namely, we have identified steps in our analysis which would limit statistics or contaminate the simulation sample with events which our algorithm is not equipped to reconstruct accurately.

More work must be done to fully understand some of the results obtained when comparing our simulation to data. This is especially true for the large discrepancy noted in the voxel number distribution; future work is already planned for studies into other kinematic variables that can shed light on event trajectories. Many more variables can be studied in order to make further refinements to the simulation analysis chain. Indeed, many quantities such as event photoelectron count and event breakdown into elastic and inelastic collisions were studied as part of this research, but were not included in this thesis. However, further work on the SuperFGD prototype may be limited as the collaboration focus shifts to the full SuperFGD installed at ND280, which is currently beginning to take data. It is unknown whether work on the SuperFGD will be able to effectively build off of previous work done on the prototype. In either case, this work will stand as a compilation of information regarding modeling neutron interactions through simulation.

Bibliography

[1] T2k illustration. /urlhttps://www.ppd.stfc.ac.uk/Pages/T2K.aspx.

[2] Aoi Eguchi. The t2k near detector upgrade. *Physical Sciences Forum*, 8 (1), 2023. ISSN 2673-9984. doi: 10.3390/psf2023008038. URL `https://www.mdpi.com/2673-9984/8/1/38`.

[3] New nd280 setup illustration. /urlhttps://t2k-experiment.org/beyond-t2k/.

[4] N. J. Carron. *An Introduction to the Passage of Energetic Particles through Matter*. Taylor & Francis Group, 2007.

[5] Cadmium. `https://www.nuclear-power.com/glossary/cadmium/cadmium-113-edge/`.

[6] W. Udo Schroder. `https://www.sas.rochester.edu/chm/courses/chm246_446/index.html`.

[7] B. V. Carlson. The optical model. In *Joint ICTP-IAEA Workshop on Nuclear Reaction Data for Advanced Reactor Technologies*, 2010.

[8] W. R. Leo. *Techniques for Nuclear and Particle Physics Experiments*. Springer-Verlag, 1987.

[9] Y. Watanabe, K. Kosako, S. Kunieda, S. Chiba, R. Fujimoto, H. Harada, M. Kawai, F. Maekawa, T. Murata, H. Nakashima, K. Niita, N. Shigyo, S. Shimakawa, N. Yamano, and T. Fukahori. Status of jendl high energy file. *Journal of the Korean Physical Society*, 59(23):1040–1045, August 2011. ISSN 0374-4884. doi: 10.3938/jkps.59.1040.

[10] B. Oborn A. B. Rosenfeld S. Guatelli, D. Cutajar. Introduction to the geant4 simulation toolkit. *ResearchGate*, 2011.

[11] Alberto Ribon. private correspondence.

[12] A. J. M. Plompen et al. The joint evaluated fission and fusion nuclear data library, JEFF-3.3. *Eur. Phys. J. A*, 56(7):181, 2020. doi: 10.1140/epja/s10050-020-00141-9.

[13] V. S. Barashenkov, W. Gudowski, and A. Polanski. Integral high-energy nucleon nucleus cross-sections for mathematical experiments with electronuclear facilities. In *3rd International Conference on Accelerator Driven Transmutation Technologies and Applications*, 7 1999.

[14] P. E. Hodgson. The nuclear optical model introductory overview.

[15] J. Allison et al. Recent developments in Geant4. *Nucl. Instrum. Meth. A*, 835:186–225, 2016. doi: 10.1016/j.nima.2016.06.125.

[16] D. H. Wright and M. H. Kelsey. The Geant4 Bertini Cascade. *Nucl. Instrum. Meth. A*, 804:175–188, 2015. doi: 10.1016/j.nima.2015.09.058.

[17] A. Boudard, J. Cugnon, J.-C. David, S. Leray, and D. Mancusi. New potentialities of the liège intranuclear cascade model for reactions induced by nucleons and light charged particles. *Phys. Rev. C*, 87:014606, Jan 2013. doi: 10.1103/PhysRevC.87.014606. URL `https://link.aps.org/doi/10.1103/PhysRevC.87.014606`.

[18] Y. Yariv. Intra-nuclear cascade model. In *International Topical Meeting on Nuclear Research, Applications and Utilization of Accelerators*, 2009.

[19] K. Abe et al. T2K ND280 Upgrade - Technical Design Report. 1 2019.

[20] Glen F. Knoll. *Radiation Detection and Measurement*. John Wiley & Sons, 1999.

[21] C. Riccio. Total neutron cross-section measurement on ch with a novel 3d-projection scintillator detector. Presented at HEP seminar at Stony Brook University, 2022.

[22] A. Blondel et al. The SuperFGD Prototype Charged Particle Beam Tests. *JINST*, 15(12):P12003, 2020. doi: 10.1088/1748-0221/15/12/P12003.

[23] Ciro Riccio et al. Total Neutron Cross-Section Measurement on CH with a Novel 3D-Projection Scintillator Detector. *Phys. Sci. Forum*, 8(1):29, 2023. doi: 10.3390/psf2023008029.

[24] I. Alekseev et al. SuperFGD prototype time resolution studies. *JINST*, 18(01):P01012, 2023. doi: 10.1088/1748-0221/18/01/P01012.

[25] L. Munteanu, S. Suvorov, S. Dolan, D. Sgalaberna, S. Bolognesi, S. Manly, G. Yang, C. Giganti, K. Iwamoto, and C. Jesús-Valls. New method for an improved antineutrino energy reconstruction with charged-current interactions in next-generation detectors. *Phys. Rev. D*, 101(9):092003, 2020. doi: 10.1103/PhysRevD.101.092003.

[26] edep-sim: An energy deposition simulation. `https://github.com/ClarkMcGrew/edep-sim`.